Detailed equilibrium and dynamical tides: impact on circularization and synchronization in open clusters

Giovanni M. Mirouh [1,2]★ David D. Hendriks,[1] Sophie Dykes,[1] Maxwell Moe [3] and Robert G. Izzard [1]

[1]*Astrophysics Research Group, Faculty of Engineering and Physical Sciences, University of Surrey, Guildford GU2 7XH, UK*
[2]*Física Teórica y del Cosmos Department, Universidad de Granada, Campus de Fuentenueva s/n, 18071, Granada, Spain*
[3]*Steward Observatory, University of Arizona, 933 N. Cherry Ave., Tucson, AZ 85721, USA*

ABSTRACT

Binary stars evolve into chemically peculiar objects and are a major driver of the galactic enrichment of heavy elements. During their evolution they undergo interactions, including tides, that circularize orbits and synchronize stellar spins, impacting both individual systems and stellar populations. Using Zahn's tidal theory and MESA main-sequence model grids, we derive the governing parameters λ_{lm} and E_2, and implement them in the new MINT library of the stellar population code BINARY_C. Our MINT equilibrium tides are two to five times more efficient than the ubiquitous BSE prescriptions, while the radiative-tide efficiency drops sharply with increasing age. We also implement precise initial distributions based on bias-corrected observations. We assess the impact of tides and initial orbital-parameter distributions on circularization and synchronization in eight open clusters, comparing synthetic populations and observations through a bootstrapping method. We find that changing the tidal prescription yields no statistically significant improvement as both calculations typically lie within 0.5σ. The initial distribution, especially the primordial concentration of systems at $\log_{10}(P/d) \approx 0.8$, $e \approx 0.05$ dominates the statistics even when artificially increasing tidal strength. This confirms the inefficiency of tides on the main sequence and shows that constraining tidal-efficiency parameters using the $e - \log_{10}(P/d)$ distribution alone is difficult or impossible. Orbital synchronization carries a more striking age-dependent signature of tidal interactions. In M35 we find twice as many synchronized rotators in our MINT calculation as with BSE. This measure of tidal efficiency is verifiable with combined measurements of orbital parameters and stellar spins.

Key words: stars: evolution – stars: rotation – open clusters and associations: general.

1 INTRODUCTION

Multiple systems are commonplace among observed stars: about 35 per cent of solar-type stars are in multiple systems, this fraction rising to more than 70 per cent in O-type stars (Sana et al. 2012; Moe & Di Stefano 2017). The presence of a companion can have a significant impact on the evolution of both stars and is necessary to explain many astrophysical events and the generation of carbon-enhanced metal-poor (CEMP) and barium stars, fast rotators, X-ray binaries, novae etc. (De Marco & Izzard 2017). Tides circularize and shrink orbits, while stellar rotation rates synchronize with the orbit, making them a crucial ingredient of binary evolution. Studying stellar populations also offers a way to constrain tides. Notably, open clusters are coeval populations of isolated binary systems; numerous measurements of their orbital parameters make them an interesting laboratory to assess when and how efficiently tides act. This work thus focuses on the derivation of accurate tidal dissipations on the main sequence, which are expected to modify the orbital parameters of stellar systems, and the study of both individual binary systems and stellar populations.

Tides in binary systems are divided into two components: the equilibrium tide and the dynamical tide (we refer the reader to the reviews by Zahn 2008 and Ogilvie 2014). The equilibrium tide results from the distortion induced by the companion's gravitational pull. The resulting bulge rotates with the star inducing dissipation through friction. This mechanism is efficient in stars with an outer convective envelope (Zahn 1977, 1989). The dynamical tide results from the generation of tidally excited, low-frequency gravity modes of oscillation at the core-boundary interface. These oscillations have periods comparable to that of the orbit. Resonances thus extract energy from the orbit that is then dissipated in the stellar envelope through radiative dissipation or in dissipative shear layers (Zahn 1970, 1975). To be efficient, dynamical tides require a convective core surrounded by a radiative layer that might in turn be surrounded by an outer convective zone. Both tidal mechanisms extract energy from the orbit, resulting in secular changes in the orbital period P, eccentricity e, and stellar rotation rates Ω. In the absence of other interactions, tides typically circularize orbits ($e \rightarrow 0$), while each star tends to spin-orbit pseudo-synchronization (Hut 1981). As systems evolve, close systems circularize first. In coeval populations, the period at which no eccentric systems exist – the cut-off period – increases over time (Witte & Savonije 2002). In open clusters in which the age is determined through turn-off fitting, the cut-off period provides an observational estimate of the efficiency of tides (Meibom & Mathieu 2005). Numerous theoretical formalisms have been developed to explain the observed period distributions of binary systems in open clusters. Much of this progress happened over the last decade,

★ E-mail: gmm@ugr.es

reopening a question that is very much in flux. It is also unclear whether binary stars formed in clusters carry a signature of their birth conditions. To test both these aspects, we present here a derivation of time-dependent tides based on detailed stellar structures that we implement in the BINARY_C binary evolution code to compute high-resolution synthetic populations of a variety of open clusters. We compute tidal time-scales following Zahn's theory (Zahn 1970, 1975, 1977, 1989). This theory introduces a formalism for both equilibrium and dynamical tides, relating the circularization and synchronization time-scales to structure quantities in both stars, most importantly the coefficients λ_{lm} and E_2 whose derivation we summarize in this work. The resulting time-scales are then used in the equations for the secular evolution of orbital parameters given by Hut (1981).

We use the BINARY_C stellar population synthesis code (Izzard et al. 2004b, 2006, 2009, 2018) to investigate individual systems and compute populations. Since its inception, BINARY_C has been regularly updated to include new physics such as nucleosynthesis, improved Roche lobe overflow prescriptions, or rotation (Izzard et al. 2018, and references therein). The rapid evolution algorithm in BINARY_C relies on the ubiquitous BSE parameters obtained through a series of fits obtained from stellar models (Hurley, Pols & Tout 2000; Hurley, Tout & Pols 2002). These fitting relations of the stellar mass and age allow for the rapid evolution of single and binary stars. In our latest developments of BINARY_C that we call MINT (for *Multi-object INTerpolation*), we implement a new interpolation approach based on grids of models over an extensive range of masses and metallicities. These grids include all the parameters necessary for the main-sequence evolution, including tides and nucleosynthesis, and are constructed with the MESA stellar evolution code (Paxton et al. 2011, 2013, 2015, 2018, 2019). For each model we calculate the relevant tidal coefficients for both kinds of tides following the formalism laid out in Zahn (1977), Hut (1981), Zahn (1989), and Siess et al. (2013). This overhaul of the evolution algorithm will be extended to later stages of evolution in upcoming papers. We use stellar populations obtained with BINARY_C to study both circularization and synchronization processes. We investigate eight open clusters that span ages from 4 Myr to 7 Gyr and contain a number of binary systems whose orbital parameters have been measured. We assess the agreement between our model cluster populations and corresponding observations through a dedicated bootstrapping method, before discussing the use of stellar rotation rates and spin-orbit synchronicity as a possible measure of tidal efficiency. Throughout this work, we focus on comparing the BSE and MINT implementations of equilibrium and dynamical tides to observations.

The paper is structured as follows. We present and justify our prescription for tides and detail the differences between the BSE and MINT implementations on the evolution of tidal parameters in selected systems in Section 2. In Sections 3 and 4, respectively, we investigate the circularization and synchronization properties of stellar populations. We then discuss the implications of our new tidal implementation in Section 5 and summarize our main findings in Section 6. Appendices provide mathematical details (Appendix A) and plots of the computed populations (Appendix B).

2 DERIVATION OF THE TIDAL PRESCRIPTIONS

In this section, we introduce the Zahn formalism of tides that we adopt and its implications, while technical details are provided in Appendix A. To assess the impact of tides on the orbital evolution of binary stars, we compute the required tidal coefficients from detailed structures obtained with MESA. We present these models and

give an overview of the numerical implementation in the BINARY_C population code.

We also discuss an experiment in which we run a series of systems with different initial spin and orbital periods to compare the efficiency of BSE and MINT tides for different initial masses and rotation rates.

2.1 Our choice of prescriptions: Zahn's formalism

In this work, we replace the BSE tide prescriptions provided by Hurley et al. (2002) with the derivation of Zahn (1970, 1975, 1977, 1989) and Hut (1981). Despite what the chronology of these works suggests, the BSE prescriptions are actually a simplification of Zahn's. Most notably, BSE underestimates tides in close systems by several orders of magnitude, while their radiative tide implementation is age-independent and overestimates tidal dissipation as stars evolve on the main-sequence.

The search for more accurate circularization has led to the development of many formalisms for both equilibrium and dynamical tides. Dynamical tide efficiency is directly related to the rate at which oscillations dissipate energy in the stellar envelope. The advent of asteroseismology has logically ushered an outburst of new calculations for dynamical tides (Willems, van Hoolst & Smeyers 2003; Burkart et al. 2012). Works such as Terquem et al. (1998), Ogilvie & Lin (2007), or Barker (2020) suggest that damped internal gravity waves extract energy from the orbit, while others invoke tidally forced inertial waves in near-synchronicity systems (e.g. Barker 2021). However, the time-scales upon which tidal forcing takes place are relatively short, and the coupling itself is quite weak (Terquem et al. 1998), unless stellar evolution somewhat maintains this forcing (through so-called resonance locking, e.g. Savonije & Papaloizou 1984; Witte & Savonije 2002; Ma & Fuller 2021). While resonance-locking increases dissipation during the pre-main-sequence (PMS), it is unclear whether it accelerates circularization on the main sequence significantly (Zanazzi & Wu 2021).

The equilibrium tide mostly relies on the amount of friction in the stellar convective envelope. Estimates vary wildly, for instance in the short-period limit (Goldreich & Nicholson 1977; Vidal & Barker 2020, a specific case we discuss in Appendix A). Terquem (2021) and Terquem & Martin (2021) recently suggested that dissipation due to turbulent convection could increase tidal efficiency, but this idea has been debated since (notably by the rebuttal of Barker & Astoul 2021), while other works emphasize the role of a magnetic field in increasing dissipation (e.g. Wei 2022). A promising study by Barker (2022) investigates the impact of inertial wave dissipation in convective envelopes on equilibrium tides, through calculations similar to those underlying dynamical tides: their frequency-averaged dissipation rate seems to yield a good agreement with observations in systems close to spin-orbit synchronization.

The tension between those different theoretical estimates leads to a rapidly changing landscape of tidal theories. However, recent works rely on the derivation of the entire oscillation spectrum of the stars considered. The systematic study of oscillation spectra over the range of masses and metallicities necessary for this study is a very ambitious work, even with current computational means, and will surely be at the core of highly anticipated future work. It is worth noting that these formalisms do not yield results qualitatively different from the formalism we implement as the conclusions we derive will show (Terquem & Martin 2021; Zanazzi & Wu 2021).

As the population synthesis calculations we perform require rapid inferences over an extended parameter range, we implement Zahn's prescriptions in MINT to derive circularization and synchronization coefficients owing to their tractability. Despite the development of

new formalisms, this is the first implementation of the prescriptions laid out in Zahn (1989) for population synthesis. The coefficients thus derived are used in the BINARY_C code in conjunction with the equations from Hut (1981) which are necessary to compute the secular evolution of systems, notably at high eccentricities ($e > 0.3$, Terquem & Martin 2021).

2.2 Our grids of MESA models

Our derivation of the tidal time-scales relies on grids of models of main-sequence stars constructed using the MESA stellar evolution code, version 12115. We use the dE/dt form of the energy equation paired with gold tolerances, along with both DT2 and ELM equation-of-state options and type2 opacities (Paxton et al. 2019 and references therein). All our models rely on a convective mixing length $\alpha_{MLT} = 2$, and semiconvection is treated following Langer, El Eid & Fricke (1985) with $\alpha_{sc} = 0.1$. We include step overshooting at the convective-core interface extending from $f = 0.05H_p$ inside the convection zone and of thickness $f_0 = 0.33H_p$ with the same diffusion coefficient as convection (based on the Solar value of Christensen-Dalsgaard et al. 2011). We cover the 0.32–100 M$_\odot$ mass range at metallicities $Z = 0$, 10^{-4}, 0.008, 0.012, and 0.016, and the extended range 0.1–320 M$_\odot$ at $Z = 0.02$. Assuming a reference of $Z = 0.02$, $Y = 0.28$ and following the solar mixture of Grevesse & Sauval (1998), we include Galactic chemical enrichment using dY/d$Z = 2$ (Serenelli & Basu 2010).

Among crucial parameters for tides, the stability of the stellar layers to convection indicates whether equilibrium or radiative tides dominate. Fig. 1 shows the distribution of stars featuring a convective envelope, in which equilibrium tides dissipate energy, and stars with a convective core in which dynamical tides act. At low metallicities, we find stars that are fully radiative on the main sequence as their convective core disappears. Zahn's formalism does not provide a description of tidal dissipation in such stars. A mechanism that relies neither on stochastically excited oscillations nor on main flow viscous dissipation is needed. Tassoul (1987, 1988) offers such a mechanism that relies on viscous near-surface boundary-layer dissipation, but its existence is controversial (Rieutord 1992; Rieutord & Zahn 1997). We decide to neglect it, meaning no tidal dissipation is taken into account in our models of these fully radiative stars at low metallicity. However, we emphasize that none of the model populations we discuss in this work include such stars.

2.3 Implementation in BINARY_C

Implementing the new tidal prescription in the BINARY_C stellar population synthesis code (Izzard et al. 2004b, 2006, 2009, 2018) is part of a larger overhaul of the code we call MINT. This change in the algorithm will be the focus of future papers, but we summarize it here. To increase the accuracy of the algorithm that derives stellar parameters used in the code, we replace BSE fitting relations (Hurley et al. 2000; Hurley et al. 2002) with regularly spaced grids of MESA models that are interpolated linearly. This still allows BINARY_C to rapidly compute populations as structures are not computed on the fly. Among the parameters available in the grids, the coefficients E and E_2 yield λ_{lm} and $(k/T)_c$ following equation (A14). Once these coefficients are calculated, they are used in the Hut (1981) equations that govern the evolution of orbital parameters and allow for accurate calculations of the secular evolution of binary systems for all eccentricities. This change is modular, allowing us to swap easily between BSE and MINT evolution algorithms and tidal prescriptions. For each population, the
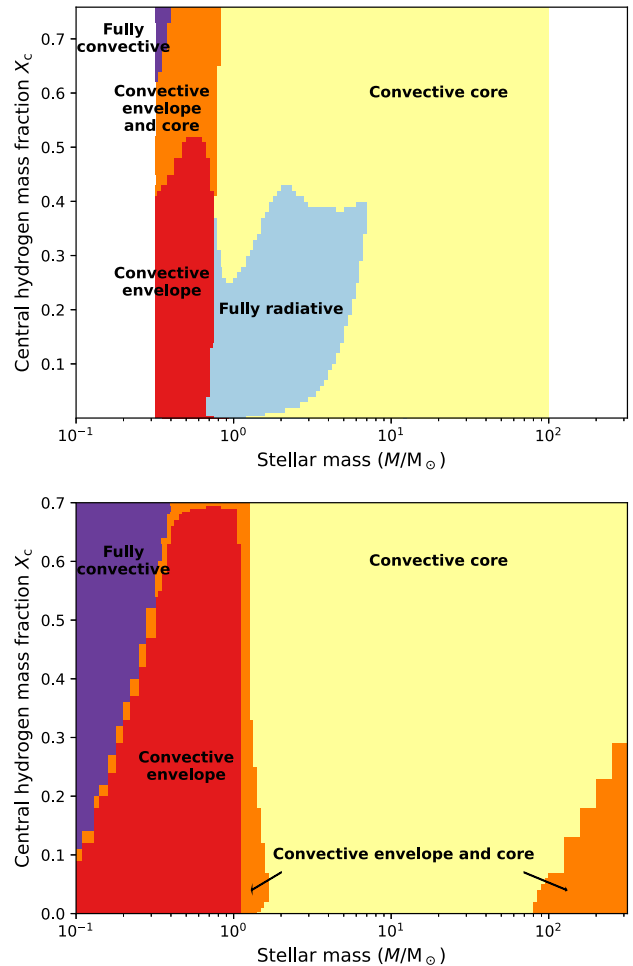

Figure 1. Location of convective regions in stars of metallicities $Z = 0$ (top) and 0.02 (bottom), as a function of mass and central hydrogen abundance. The zero-age main sequence is at the top of each panel and evolution proceeds vertically downwards. Colours denote fully convective (purple) or fully radiative (blue) stars, or the presence of a convective core (yellow), a convective envelope (red), or both a convective core and a convective envelope separated by a radiative shell (orange). Stars with a convective surface (red, orange, and purple) harbour equilibrium tides, while stars with a radiative zone around a convective core (orange and yellow) harbour dynamical tides.

computation, output management, and data storage is performed with the BINARY_C-PYTHON software package (Hendriks & Izzard 2023).

2.4 Our choice of initial orbital parameters: Moe & di Stefano (2017)

In this work, we implement empirical zero-age main-sequence orbital parameter distributions. Unless otherwise specified, we use a Kroupa (2001) initial mass function in conjunction with initial distributions of the mass ratio, eccentricity, and period from Moe & Di Stefano (2017). Relying on ∼30 observational surveys based on a variety of techniques, Moe & Di Stefano (2017) performs a careful correction of observational biases to provide initial binary parameters distributions. Their study includes stars from the field and from both solar-like and massive star open clusters to provide tabulated probability functions of the mass ratio, period, and eccentricity. This empirical distribution arises from the interaction of Kozai–Lidov

cycles, dynamical instabilities, and tidal friction during the PMS evolution (Moe & Kratter 2018).

2.5 Main properties of our new implementation

The MINT overhaul of BINARY_C includes changes to both the stellar evolution algorithm and tides. We find that the changes in the algorithm from BSE to MINT do not significantly affect the main-sequence evolution of the stellar structure (e.g. radius and luminosity), but the MINT tides induce strong differences on the secular orbital parameter evolution. We assess these differences through simple experiments we summarize here.

2.5.1 Efficiency of MINT and BSE tide circularization

We evolve a set of binary systems with initial eccentricity $e = 0.6$ and a range of initial orbital periods until they exchange mass or leave the main sequence, whichever comes first. Evolving these systems starting at masses $M_1 = 1 \, M_\odot$, $M_2 = 0.5 \, M_\odot$, and a rotation rate of $10^{-4} \, \text{km s}^{-1}$ for 100 Myr, we find that MINT equilibrium tides circularize all systems with orbital periods shorter than $P \sim 3$ d, while BSE tides circularize systems with orbital periods shorter than $P = 0.9$ d. Over the whole main-sequence evolution, MINT tides circularize systems up to $P = 15$ d, while BSE tides circularize systems up to $P = 6$ d. This comparison shows that MINT equilibrium tides are more efficient than their BSE counterparts, circularizing orbits in solar-like binaries more rapidly and affecting relatively longer period systems.

We repeat the same experiment in systems starting at masses $M_1 = 50 \, M_\odot$ and $M_2 = 25 \, M_\odot$, at $e = 0.6$ and initial rotation rate of $10^{-4} \, \text{km s}^{-1}$. In this case, BSE dynamical tides circularize systems with $P < 8$ d over the first Myr, while their MINT counterparts circularize systems with $P < 5$ d. Over the whole main-sequence, circularized systems reach $P = 25$ d with BSE tides and $P = 8$ d with MINT tides. Systems with a longer orbital period also see their orbit expand near the zero-age main sequence (ZAMS) owing to stellar winds. This experiment confirms that MINT dynamical tides are less efficient than BSE's. Mathematically, this matches the behaviour of the E_2 coefficient: while on the ZAMS it is similar in both prescriptions, it remains constant in the BSE calculation but drops significantly in the MINT prescription. This effect is shown in Fig. A8. Age-dependent radiative tides have been used in Yoon, Woosley & Langer (2010), Siess et al. (2013), and Qin et al. (2018); we provide a comparison with these calculations in Fig. A9.

2.5.2 Impact of the initial rotation rate

We repeat the above experiment at $M_1 = 1 \, M_\odot$, $M_2 = 0.5 \, M_\odot$ but vary the initial rotation rate. We consider four of the BINARY_C possible settings: (i) a very low rotation rate of $10^{-4} \, \text{km s}^{-1}$ that is equivalent to no rotation, (ii) spin-orbit synchronicity, (iii) breakup, and (iv) with the BSE mass-dependent initial rotation rate defined as

$$v_{\text{rot}}(M) = \frac{330 M^{3.3}}{15 + M^{3.45}} \, \text{km s}^{-1}, \qquad (1)$$

for a given mass M expressed in Solar units (Lang 1992; Hurley et al. 2000). We find no significant impact of the initial rotation on the evolution of orbital parameters, with circularization happening only slightly faster when the stars rotate more slowly.

The most notable feature of these tracks concerns systems formed with both stars at breakup velocity with $0.2 < \log(P/d) < 0.9$. They

present a short-lived eccentricity pumping phase on the early main sequence. This can be traced to equation (10) of Hut (1981), in which equilibrium tides provide a positive contribution to the eccentricity derivative if the stellar angular frequency exceeds the orbital angular frequency by a factor 5 to 10. However, stars undergo magnetic breaking during the PMS phase and are not expected to reach the ZAMS at breakup velocities. We do not include the PMS in MINT, but our main-sequence evolution includes magnetic braking through the prescription of Andronov, Pinsonneault & Sills (2003) which is calibrated on open cluster data and predicts angular momentum loss scaling with Ω^3.

3 POPULATION SYNTHESIS AND COMPARISON TO CLUSTER OBSERVATIONS

Binary systems in stellar clusters form with a distribution of initial masses, eccentricities, and orbital periods. These stars then evolve through stellar evolutionary stages while their orbits circularize through tides. As equations (A1)–(A2) and (A15)–(A16) show, close-period systems circularize first, so that we observe a dichotomy between close, circular, and wide, eccentric systems. We can define a cut-off period below which all systems are circular by studying the distribution of binary systems in the $e - \log_{10}(P/d)$ plane. As this cut-off period increases with the cluster's age, it can be used to infer the age of the population (Witte & Savonije 2002).

In this section, we study a sample of open clusters containing binary systems for which orbital parameters have been measured. We focus on open clusters that have a lower stellar density than globular clusters, thus minimizing the role of N-body interactions. We compute synthetic populations matching these clusters with BINARY_C to test initial populations and tidal prescriptions through their impact on the circularization process.

3.1 Model populations with BINARY_C

We compute populations evolving a high number of stars and systems from a given metallicity and initial orbital-parameter distribution. Each system is evolved using BINARY_C, relying on either BSE parameters or the interpolation of MINT grids. We stop the calculation slightly after the documented cluster age and investigate the eccentricity and orbital period of binary orbits, along with the stellar rotation rates. The parameter space for these quantities is divided into bins in which we add the fractional number of stars for each system at each time-step. In the model populations we present here, we use 950 000 stars for which we track the orbital period, eccentricity, and stellar spins in units of the critical and pseudo-synchronous rotation rates. We store these quantities in bins of sizes 0.1 for $\log_{10}(P/d)$ and $\log_{10}(\Omega/\Omega_{\text{sync}})$, and 0.02 for e and $\Omega/\Omega_{\text{crit}}$. To emphasize the dominant structure of our model populations, we apply a Gaussian smoothing to the two-dimensional distributions presented in the figures of this section and the next. This smoothing uses widths six and three times the bin sizes on the horizontal and vertical axes, respectively, and is applied after the statistical calculations we discuss.

3.2 Goodness-of-fit tests

Our model populations provide a distribution of the fractional number of stars, for instance in the $e - \log_{10}(P/d)$ plane, that we interpret as a likelihood map. To decide whether a set of observations could be drawn from the synthetic population, we bootstrap two samples from this likelihood map, whose size matches the number of observed stars
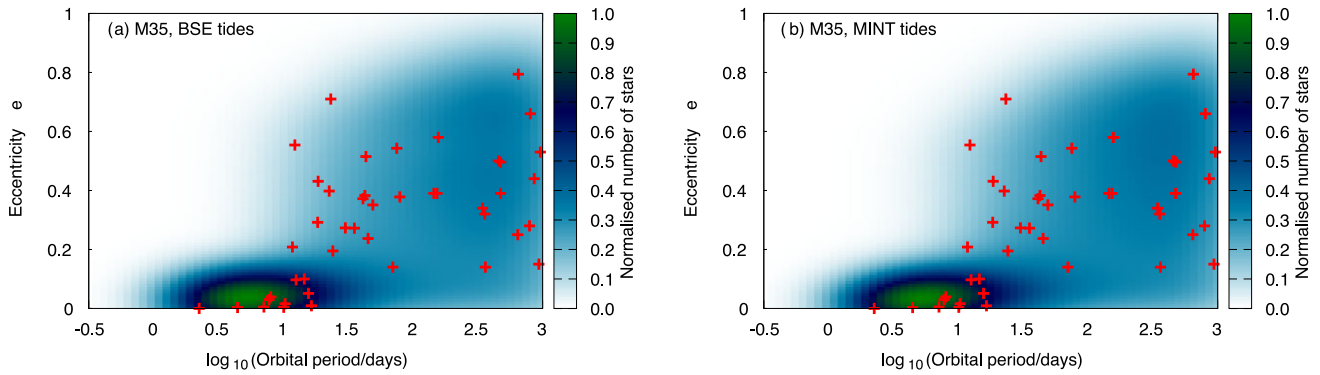
Figure 2. Comparison between M35 observations (red crosses) and the stellar counts calculated populations at 150 Myr normalized at the highest bin count (colour map). Starting with initial distributions from Moe & Di Stefano ([2017](#)), we use tides from BSE (a) and our MINT tides (b).

for the cluster and period range considered. We assess the statistical distance between each of these samples and observations, and between the two samples, through a two-dimensional Kolmogorov–Smirnov test (KS test, Peacock [1983](#); Fasano & Franceschini [1987](#)).

This well-established test is a generalization of the one-dimensional KS process (Stephens [1992](#)) to two dimensions. The two-sample 1D KS test relies on the cumulative distribution function of two samples: the statistical distance between the two samples is defined as the maximum difference between their cumulative distribution functions, and is directly related to the probability of the two samples being extracted from a same distribution.

In two dimensions, the key step is to replace the 1D cumulative distribution function with similar functions computed over the 2D plane by splitting it into the four natural quadrants around a given point (x_i, y_i),

$$(x > x_i, y > y_i), (x < x_i, y > y_i), (x > x_i, y < y_i),$$
$$(x < x_i, y < y_i).$$

Each quadrant contains part of the samples, yielding cumulative distribution functions that we compare. The statistical distance is taken as the largest of the differences between these functions for each of the samples. Fasano & Franceschini ([1987](#)) have shown that this process yields robust inferences when restricting the choice of (x_i, y_i) to the data points in the samples. From the statistical distances, it is then possible to retrieve the probability of the two samples being extracted from the same underlying population through equations (3), (7), (8), and (9) of Press & Teukolsky ([1988](#)).

In this work, we keep our focus on the statistical distances inferred from these tests. First, the statistical distance between the two bootstrapped samples yields the minimum distance attainable through the KS test. This minimum distance follows a Poisson law and serves as a reference value, which we label as the 'distance to self' in the rest of this work. The same estimator is then used to assess the statistical distance between each of the two samples and the observed parameters to assess the agreement between observed and model populations. The distance thus obtained is, by definition, larger than the Poisson reference.

We repeat this process 1000 times, both for the Poisson reference and the model–observation statistical distances. These distance estimates distribute over a Gaussian for which we compute a mean and standard deviation σ. For the populations computed for M35 and shown in Fig. [2](#), the bell-shaped spread of the distances is illustrated on Fig. [3](#), which presents a histogram of the distances in

bins whose width is represented in the top-right corner. The closer the model–observation distance (dashed lines) is to the Poisson reference distance (black line), the more likely the agreement between the observed and model populations.

As can be seen in Fig. [2](#), the agreement between observations and our model populations is driven by two populations: short-period circular systems and long-period eccentric systems. In order to isolate the circularization process, we compute the statistical agreement over the whole population and over a short-period subset, by imposing a cut-off on $\log_{10}(P/\mathrm{d})$ that depends on the cluster. It is important to notice that the common sample size N affects both the distances and their standard deviations we compute, as they all scale with $\sqrt{N}$: we will thus discuss the agreement between our populations in units of σ.

This approach is fundamentally different from the definition of a cut-off period to estimate tidal efficiency, as was done in e.g. Meibom & Mathieu ([2005](#)). Other studies, such as Zanazzi ([2022](#)) or Bashi, Mazeh & Faigler ([2023](#)), extend that cut-off period approach by studying the evolution of eccentricity through two characteristic periods: one for circular systems and one for more eccentric, longer period systems. Applying this dichotomic approach to large samples (hundreds or thousands of systems) yields crucial statistical insights into tidal efficiency. In this work, we do not perform such separation when computing KS distances. However, even though the clusters we consider do not feature such numbers of binary systems, an exploration of the distinct statistics of circular and eccentric systems with our bootstrapping approach will be the focus of future work.

3.3 Our first study case: the cluster M35

3.3.1 Impact of the tidal prescription

Leiner et al. ([2015](#)) present observations of the M35 cluster, a 150 Myr old cluster with metallicity [Fe/H] = −0.18. 52 binary systems are detected with periods 2–4400 d, covering a wide range of eccentricities. Both stars in each system are on the main sequence, with primary star masses 0.7–1.4 $M_\odot$ and no significant information about the mass ratio derived from the observations (Meibom & Mathieu [2005](#)). This cluster presents the signature of circularization processes, with a clear transition from eccentric systems at periods longer than ∼10 d to only circular orbits at shorter periods. As such, it is a good test case for our tidal implementation. In this section we present our population calculations with BINARY_C comparing MINT and BSE tides. Starting from the initial parameter distributions
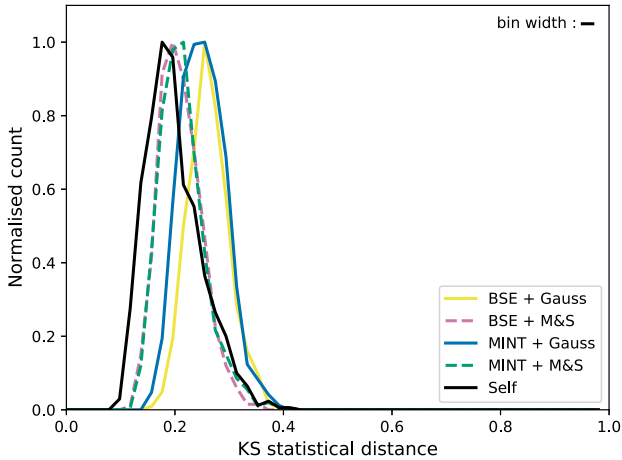
Figure 3. Kolmogorov–Smirnov (KS) statistical distance between the whole set of M35 observations and our corresponding model populations. Each coloured line indicates the distance between a model population obtained from a physical set-up and the observations. Set-ups include BSE and MINT tides starting from Moe & di Stefano distributions (M&S, dashed pink and green, respectively, see Fig. 2), and BSE and MINT tides starting from Gaussian distributions (solid yellow and blue, respectively, see Fig. 5). The black curve denotes the reference Poisson distance obtained using random samples from one model population. The black line in the top-right corner corresponds to the model bin width. The statistical mean and standard deviation obtained from these distances are reported in Table 1.

Figure 4. As Fig. 3 restricting the calculation to the subset of data with $\log_{10}(P/\text{d}) < 1.7$. The statistical mean and standard deviation obtained from these distances are reported in Table 1.

Table 1. Kolmogorov–Smirnov statistical distance estimates for the M35 model populations starting from Moe & di Stefano distributions, for BSE or MINT tides, for the entire sample or a subset at $\log_{10}(P/\text{d}) < 1.7$.

Cluster and $\log_{10}(P/\text{d})$ range	Tides	Distance to self	Distance to obs
M35	BSE	0.208 ± 0.046	0.220 ± 0.038
entire sample	MINT	0.209 ± 0.050	0.224 ± 0.041
M35	BSE	0.290 ± 0.072	0.396 ± 0.075
$\log_{10}(P/\text{d}) < 1.7$	MINT	0.288 ± 0.066	0.392 ± 0.078

In both cases, we find that our model populations are compatible with the observations. We find no statistically significant difference between the BSE and MINT prescriptions. This seems to show that the initial orbital parameter distribution dominates the circularization distribution on the main sequence. This is due to the Moe & di Stefano distribution having a clump of short-period low-eccentricity systems (centred on $\log_{10}(P/\text{d}) = 0.8$, $e = 0.05$) that roughly matches the location of observed circular systems.

3.3.2 Impact of the initial parameter distributions

To further assess this last hypothesis, we compute populations starting from a different, more simple set of initial orbital parameters that do not include a short-period, low-eccentricity clump. For this test, we use the initial parameters suggested by Duquennoy & Mayor (1991): the same Kroupa initial mass function, along with a flat mass-ratio distribution, a normal distribution of eccentricities, and a log-normal distribution of periods at age zero. The Gaussian eccentricity distribution has mean 0.35 and width 0.21, while the distribution of $\log_{10}(P/\text{d})$ has mean 4.2 and width 4.8. We insist that these Gaussian initial orbital period and eccentricity distributions are not obtained from observations but serve as a proxy for an initial population without circularized orbits, meant to study the effect of tides in isolation. Starting from these distributions, we use BSE and MINT tides to compute $e - \log_{10}(P/\text{d})$ distributions to compare with the observations. These distributions are shown in Fig. 5. We see that BSE equilibrium tides cannot account for the observed low-eccentricity short-period systems, and while MINT tides yield a small population

described in Section 2.4, we evolve the model populations to an age of 150 Myr, the age of the cluster documented in the literature.

We study the distribution of stars in the $e - \log_{10}(P/\text{d})$ plane to assess the efficiency of circularization and the agreement with observations.

Fig. 2 shows the $e - \log_{10}(P/\text{d})$ plane of M35 observations from Leiner et al. (2015) and our model distributions. The colour maps indicate the relative number of our model stars at a given location, while the red crosses are the observed locations of binary systems. Note that the number of model stars shown in each bin is relative to that of the most populated bin of either panel.

We compare the observations to our two synthetic populations obtained by changing the tidal prescription. To describe the circularization process, we compare observations and model populations through the bootstrapping method described in Section 3.2 using both the full set of observations and a subset of systems with orbital periods shorter than 50 d ($\log_{10}(P/\text{d}) < 1.7$). The corresponding distributions of the KS statistical distance are presented in Figs 3 and 4 (dashed lines), while their statistical elements are summed up in Table 1.

First, we confirm that the statistical distances obtained by comparing a computed population to itself do not depend on the underlying physics, but only on the sample size for each of the runs we have performed. It serves as a reference for our other statistical tests. Using a subset of the observations, and thus a smaller sample size for the bootstrapping process, generally yields larger distances and uncertainties but lets us assess the agreement between populations and observations.

Considering the entire period range, we find a satisfactory agreement between the observation data set and the model populations, as the two lie 0.3σ from the Poisson reference using either BSE or MINT tides. When focusing on circularizing systems at $\log_{10}(P/\text{d}) < 1.7$, the distance rises to 1.4σ.
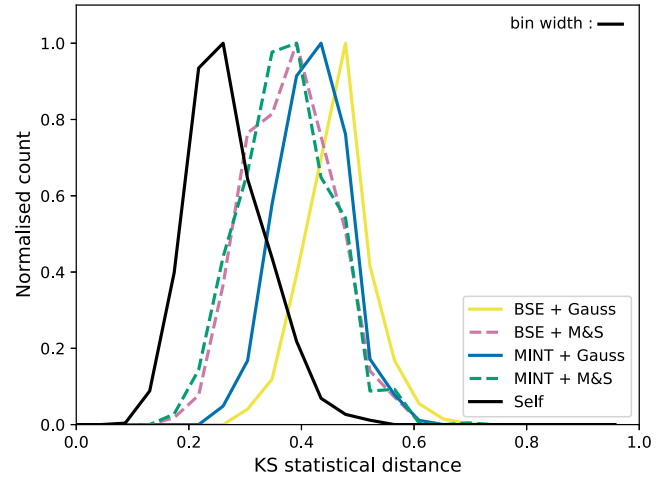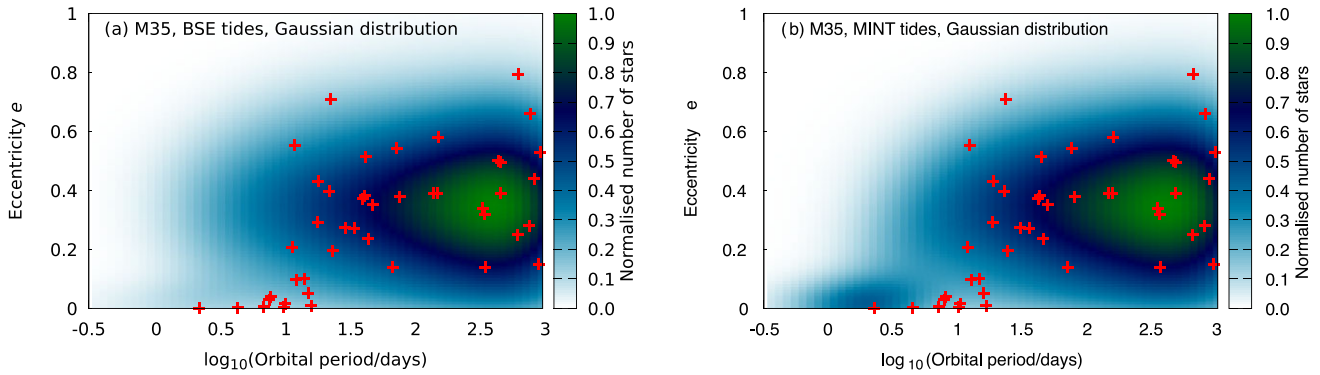
Figure 5. As Fig. 2 starting from Gaussian initial distributions.

Table 2. As Table 1, starting from Gaussian initial distributions.

Cluster and $\log_{10}(P/\text{d})$ range	Tides	Distance to self	Distance to obs
M35 entire sample	BSE	0.213 ± 0.047	0.272 ± 0.037
	MINT	0.213 ± 0.044	0.261 ± 0.040
M35 $\log_{10}(P/\text{d}) < 1.7$	BSE	0.301 ± 0.069	0.483 ± 0.064
	MINT	0.296 ± 0.067	0.436 ± 0.062

of circular close systems, the location and number of stars in this subset of the parameter space do not match the observed systems.

Gaussian initial distributions deteriorate the agreement between the observed and model populations significantly, as the statistical elements presented in Figs 3 and 4 (solid lines) and Table 2 show. For the entire sample, the statistical distance increases from 0.3σ to 1.4σ with BSE tides and to 1.1σ with MINT tides. When focussing on the short-period systems at $\log_{10}(P/\text{d}) < 1.7$, we find that the distance between observations and models increases to 2.4–2.8σ.

These distances confirm the significant impact of the Moe & Di Stefano (2017) initial distributions in improving the agreement between observed and modelled eccentricities and periods for open clusters, notably due to the primordial population of circular close systems. We find similar results for all the clusters presented in Section 3.4, but will not discuss them further owing to the unrealistic nature of the underlying Gaussian distributions.

3.4 Other clusters

After having established the method on M35, we apply it to seven other clusters for which binary populations have been observed to assess whether our updated initial orbital parameter distributions and tide prescriptions can match observations. We list these clusters and their key properties in Table 3. All but one of these clusters contain main-sequence late-type stars that we present in order of increasing age from 100 Myr to 7 Gyr. It is worth noting that while we use six clusters of late-type main-sequence stars, in which equilibrium tides are expected to dominate the circularization process, the range of masses, ages, and metallicities covered lead to a variety of internal structures and tidal coefficients. The notable exception is Tarantula, a very young cluster of O-type stars that allows us to assess dynamical tides in massive stars. In this section, we discuss the population parameters and their agreement with observations, $e - \log_{10}(P/\text{d})$ diagrams and are presented in Appendix B. The statistical elements obtained for all clusters are listed in Table 4 and shown in Fig. 6.

3.4.1 Pleiades

The Pleiades is a young, 100 Myr old stellar cluster for which observations by Mermilliod et al. (1992, 1997) provide the orbital parameters of 13 binary systems with masses from 0.9 to 1.4 $M_\odot$. It has [Fe/H] = $+0.042$ and we use $Z = 0.016$ for our model population. We compute model populations for this cluster using the same approach as for M35 and present the associated period-eccentricity distributions in Fig. B1. We compute the agreement between the computed population and the observations, following the bootstrapping method described above, for both the whole data set, and a subsample at $\log_{10}(P/\text{d}) < 1.5$.

Over the entire data set, we find that both populations lie at a distance of about 0.4σ from observations, with BSE and MINT tides lying at 0.1σ of each other. The short-period subsample we consider contains eight systems that are expected to be circularized and have

Table 3. Summary of the cluster observational information used for population synthesis.

Cluster	MS systems	Age (Gyr)	Mass range	[Fe/H]	References for observations
M35	52	0.15	$0.7 - 1.4\,M_\odot$	-0.18	Meibom & Mathieu (2005); Leiner et al. (2015)
Pleiades	13	0.1	$0.9 - 1.4\,M_\odot$	$+0.042$	Mermilliod et al. (1992); Mermilliod, Bratschi & Mayor (1997)
Hyades/Praesepe	53	0.63	$0.5 - 1.5\,M_\odot$	$+0.14, +0.21$	Griffin & Gunn (1978, 1981); Griffin, Mayor & Gunn (1982); Griffin et al. (1985)
					Mermilliod et al. (1990, 1992); Mermilliod & Mayor (1999)
NGC 7789	43	1.6	$1.4 - 1.8\,M_\odot$	$+0.02$	Nine et al. (2020)
NGC 6819	68	2.5	$1.1 - 1.6\,M_\odot$	$+0.09$	Hole et al. (2009); Milliman et al. (2014)
M67	94	4	$0.7 - 1.3\,M_\odot$	$+0.05 - +0.1$	Geller et al. (2021)
NGC 188	49	7	$0.9 - 1.14\,M_\odot$	0	Geller et al. (2009); Geller & Mathieu (2012)
Tarantula	38	~ 0.004	$20 - 80\,M_\odot$	-0.37	Almeida et al. (2017)

Table 4. Mean and standard deviation for the KS distance estimates between model and observations for all the samples considered here. All these calculations rely on Moe & di Stefano initial orbital parameters distributions.

Cluster and $\log_{10}(P/\mathrm{d})$ range	Tides	Distance to self	Distance to obs
Pleiades entire sample	BSE	0.383 ± 0.092	0.411 ± 0.090
	MINT	0.380 ± 0.090	0.416 ± 0.089
Pleiades $\log_{10}(P/\mathrm{d}) < 1.5$	BSE	0.461 ± 0.109	0.479 ± 0.090
	MINT	0.457 ± 0.109	0.470 ± 0.091
Hyades/Praesepe entire sample	BSE	0.212 ± 0.048	0.331 ± 0.058
	MINT	0.212 ± 0.048	0.341 ± 0.060
Hyades/Praesepe $\log_{10}(P/\mathrm{d}) < 1.4$	BSE	0.330 ± 0.078	0.544 ± 0.041
	MINT	0.321 ± 0.077	0.498 ± 0.045
NGC 7789 entire sample	BSE	0.223 ± 0.052	0.284 ± 0.059
	MINT	0.226 ± 0.051	0.282 ± 0.058
NGC 6819 entire sample	BSE	0.186 ± 0.042	0.228 ± 0.044
	MINT	0.185 ± 0.041	0.226 ± 0.044
NGC 6819 $\log_{10}(P/\mathrm{d}) < 1.5$	BSE	0.282 ± 0.071	0.318 ± 0.055
	MINT	0.278 ± 0.069	0.319 ± 0.055
M67 entire sample	BSE	0.160 ± 0.037	0.306 ± 0.042
	MINT	0.161 ± 0.036	0.310 ± 0.045
M67 $\log_{10}(P/\mathrm{d}) < 1.8$	BSE	0.236 ± 0.057	0.334 ± 0.050
	MINT	0.229 ± 0.056	0.302 ± 0.047
NGC 188 entire sample	BSE	0.218 ± 0.049	0.328 ± 0.060
	MINT	0.217 ± 0.048	0.329 ± 0.060
NGC 188 $\log_{10}(P/\mathrm{d}) < 1.7$	BSE	0.292 ± 0.068	0.337 ± 0.063
	MINT	0.290 ± 0.069	0.340 ± 0.065
Tarantula entire sample	BSE	0.234 ± 0.056	0.230 ± 0.045
	MINT	0.230 ± 0.055	0.239 ± 0.047

a similar behaviour, as the population computed with BSE tides lies at 1.8σ, and MINT tides lower this distance to 1.3σ.

This shows that the observations of the young Pleiades model populations bear the signature of the $\log_{10}(P/\mathrm{d}) = 0.8, e = 0.05$ clump in the initial distribution and have not been impacted by tides in a way that allows us to significantly assess the best tidal prescription from circularization. It is also crucial to note that the large standard deviations and Poisson distances in both calculations prevent a definite identification of the best candidate model population when relying on such small sample sizes.

3.4.2 Hyades/Praesepe

Hyades and Praesepe are twin supersolar clusters ([Fe/H] = +0.014 and +0.021, respectively) that formed together about 630 Myr ago. Observations from a series of articles referenced in Table 3 provide the orbital parameters of 53 systems with masses 0.5–1.5 $M_\odot$. Our model population using $Z = 0.02$ is presented in Fig. B2 This cluster is older than M35 or Pleiades, leaving more time for tides to act on close systems.

For both the MINT and BSE tides, the model populations we compute lie 2.1σ from the Poisson reference. For a subset of circularizing systems with $\log_{10}(P/\mathrm{d}) < 1.4$, neither of our model populations match the observed parameters with the best model lying 3.7σ away from the reference.

This mismatch between the observed systems and our computed populations is due to the intermediate-period eccentric systems (at $0.7 < \log_{10}(P/\mathrm{d}) < 1.2$, $e > 0.2$) that our calculations do not predict. These peculiar systems were already highlighted by Duquennoy & Mayor (1991), and impact negatively the calculation of the circularization period by Meibom & Mathieu (2005). They may be explained by the presence of an outer tertiary companion. Either through Kozai–Lidov interactions pumping the eccentricity of the inner binary (Raghavan et al. 2010) or through the interaction of
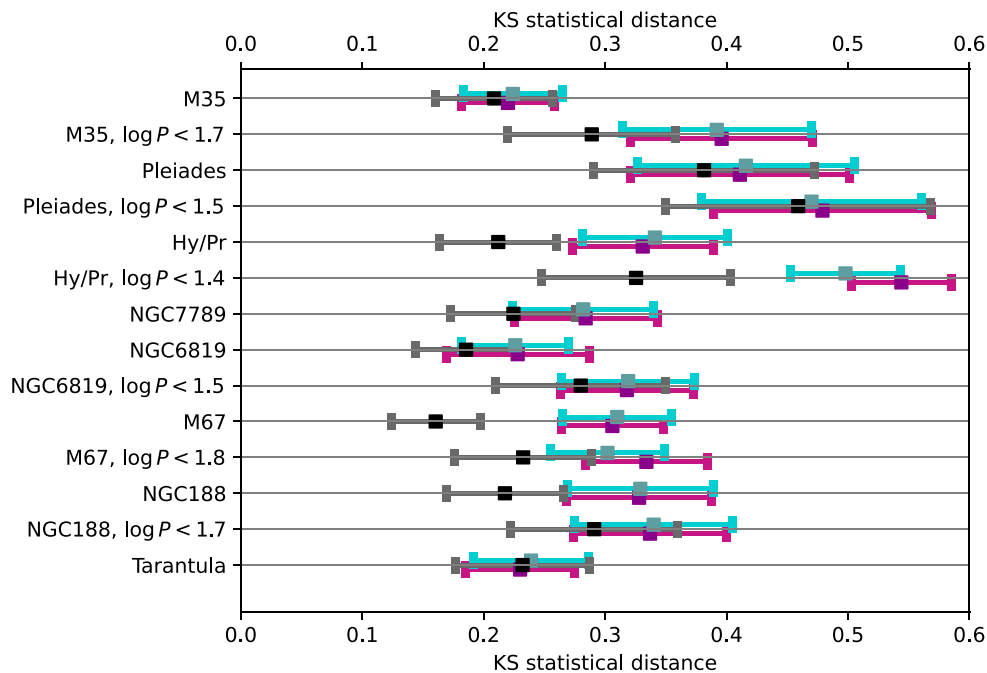
Figure 6. Mean and standard deviation for the KS distance estimates between model and observations for the samples indicated. We plot the distance to self (black), and the distance between the observations and populations computed using BSE tides (purple) and MINT tides (blue).

these Kozai–Lidov cycles with tides shrinking the orbit of originally wider systems (Moe & Kratter 2018), triple-star effects lead to intermediate-period eccentric systems that cannot be explained by binary evolution alone.

3.4.3 NGC 7789

NGC 7789, presented in Nine et al. (2020), is a 1.6 Gyr cluster with [Fe/H] = +0.02 in which 43 main-sequence stellar systems are identified in the 1.4–1.8 $M_\odot$ range (Nine, private communication). We compute a model population at $Z = 0.016$ for masses covering this range.

The distribution of our model population in the $e - \log_{10}(P/\mathrm{d})$ plane is shown in Fig. B3. This cluster contains a population of systems at $e < 0.2$, $\log_{10}(P/\mathrm{d}) < 1.2$ surrounding the location of the clump from Moe & di Stefano's initial distributions. This concentration could be attributed to tidal circularization on the main-sequence, but the statistical distance between observations and model populations is 1.7σ for both tidal prescriptions, thus showing that the agreement between the computed population and the observed parameters mostly depends on the initial conditions, as is the case for the clusters discussed previously.

3.4.4 NGC 6819

NGC 6819 (Hole et al. 2009) is slightly metal-rich with [Fe/H] = +0.09 ± 0.03 (Bragaglia et al. 2001) and age 2.4 Gyr. We resample the 68 main-sequence stars of Milliman et al. (2014) by applying cut-offs $V > 14.85$ and $0.7 < (V - I) < 0.95$ to their photometric data. The systems cover the period range $0.1 < \log_{10}(P/\mathrm{d}) < 3.6$ with primary masses 1.1–1.6$M_\odot$. We compute a model population at $Z = 0.0175$ for this range of primary masses.

Our model populations in the $e - \log_{10}(P/\mathrm{d})$ plane are shown in Fig. B4. This cluster contains a population of near-circular systems at $e < 0.1$, $\log_{10}(P/\mathrm{d}) < 1.2$ matching Moe & di Stefano's initial distributions. Comparing the whole set of observations to our computed populations, we find that the populations lie at 1σ from each other, with both BSE tides and MINT tides. Focusing the statistical inference on the circularizing systems with $\log_{10}(P/\mathrm{d}) < 1.5$ improves the agreement further, as the populations lie 0.6σ away from the observations. This confirms that the observed distribution of binary systems can be reproduced when choosing accurate initial distributions, and that the choice of tidal prescription only has a marginal impact.

3.4.5 M67

M67, also known as NGC 2682, is a 4 Gyr cluster with [Fe/H] between +0.05 and +0.1 in which 94 main-sequence binary systems are observed (Geller et al. 2021). These stars are divided between circular systems with $e < 0.05$, $\log_{10}(P/\mathrm{d}) < 1.2$ and eccentric systems with $e < 0.9$, $\log_{10}(P/\mathrm{d}) > 0.8$. They belong to the $0.7 - 1.3\,M_\odot$ range, which we use for our population study with metallicity $Z = 0.0175$.

The model populations we compute are shown in Fig. B5. We find that the agreement between our model populations and the 94 observed binary systems is not satisfactory, as it goes from 3.7σ with BSE tides to 3.3σ then using MINT tides. The relatively poor statistical agreement between our calculated populations and the observed binary systems of M67 can be attributed to the six long-period

eccentric systems ($e > 0.7$, $\log_{10}(P/\mathrm{d}) > 1.8$), whose distribution is only marginally matched in our calculations.

Selecting systems with $\log_{10}(P/\mathrm{d}) < 1.8$ confirms that the best statistical agreement is obtained using MINT tides, with model populations and observations lying 1.55σ apart.

3.4.6 NGC 188

The oldest cluster we consider is NGC 188, at an age of 7 Gyr and solar metallicity (Mathieu, Meibom & Dolan 2004). Starting from the photometry of Geller et al. (2009), we select the main-sequence stars with $V > 15$ and $0.65 < (B - V) < 0.9$ (Mathieu, private communication). This leaves us with a sample of 49 stars in the 0.9–1.14 mass range (Geller et al. 2009; Geller & Mathieu 2012), that we use for our population along with solar metallicity $Z = 0.0142$.

We present our model populations in Fig. B6. We find that the distance between all 49 observed main-sequence systems and model populations is of 2σ with both tidal prescriptions. When focusing on a subset of close systems with $\log_{10}(P/\mathrm{d}) < 1.7$, the distance drops to 0.7–0.8σ. Despite 7 Gyr of main-sequence evolution, this cluster carries a strong signature of the initial orbital parameter distribution that tides cannot dissipate.

3.4.7 Tarantula

Lastly, we consider observations of a region populated by young, massive stars, the Tarantula nebula. This dense region of the Large Magellanic Cloud formed through a series of star formation bursts 1 to 7 million years ago (Schneider et al. 2018) and has a metallicity about half-solar corresponding to $Z = 0.008$ (Tsamis & Péquignot 2005; Choudhury, Subramaniam & Piatti 2015). We focus on the 38 O stars with orbital properties from Almeida et al. (2017). We include stars in the mass range 20–80 $M_\odot$ in our model population, we use mass ratios in the range 0.5–1 to match the observations, $Z = 0.008$ and a reference age of 4 Myr. We compare our model population with observations in the $e - \log_{10}(P/\mathrm{d})$ plane in Fig. 7.

While it contains much younger and more massive stars than the previous examples we present, this cluster follows the same statistical behaviour. The agreement is excellent as our model populations match the observations with a distance below 0.2σ. The tidal prescription does not change this agreement, which is to be expected as the cluster is very young and BSE and MINT prescriptions start at a similar value, with BSE tidal coefficients remaining constant but MINT dropping over time.

3.5 Artificially modulating tides

Despite having seen in Section A1.1 that MINT tides are about ten times as efficient as BSE in most solar-like stars, the statistics of the open clusters seem to be dominated by the initial orbital distributions. To measure the effect of tides when relying on the Moe & di Stefano distributions, we modulate the efficiency of tides multiplying the orbital period and eccentricity derivatives by a multiplicative strength factor.

To assess the impact of such a multiplicative change on the match with the observations, we test strength factors from 0 to 1000. We perform this test for the young cluster M35, and for the much older M67 that has the best-quality data (Geller et al. 2021). We compare populations computed assuming Moe & di Stefano initial distributions with BSE and MINT tides, and compute the statistics of both the whole data set and the low-period subset of circularizing
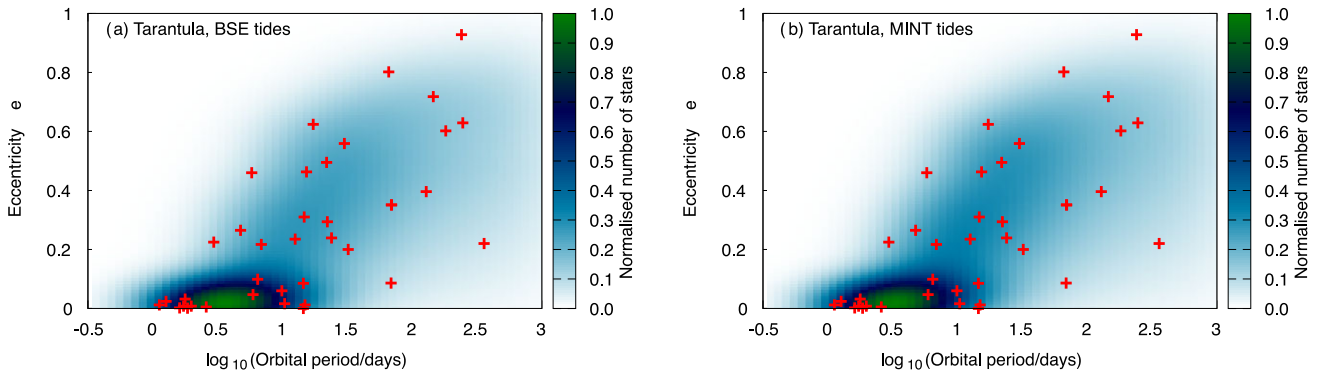
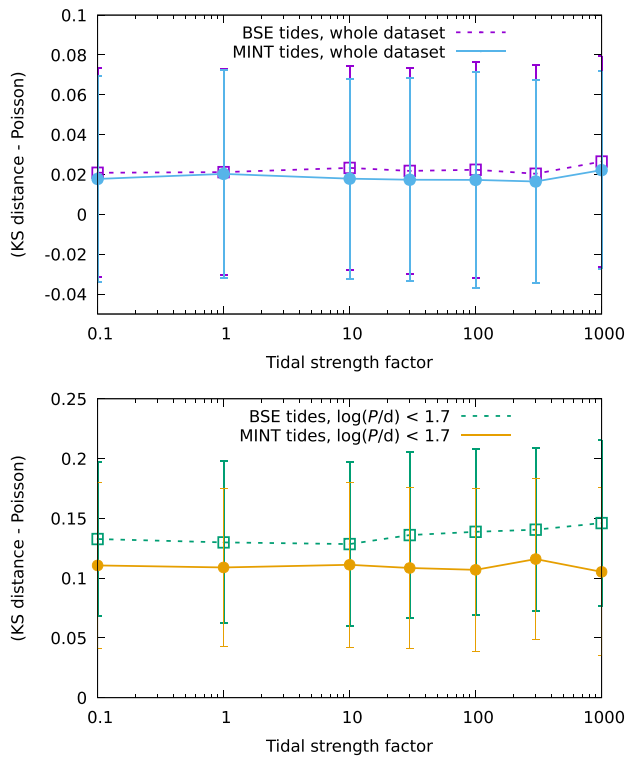**Figure 7.** As Fig. 2 for the Tarantula cluster.

Figure 8. Measure of the statistical agreement between M35 observations and populations computed with both BSE and MINT tides for various tidal strength factors, for the whole data set (top) or a subset with $\log_{10}(P/\mathrm{d}) < 1.7$ (bottom).
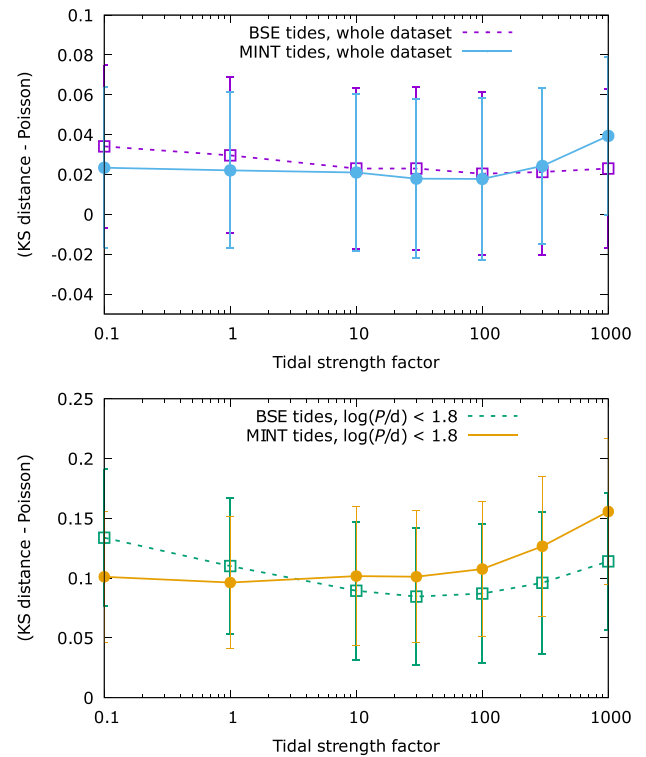
Figure 9. As Fig. 8 for the M67 cluster, for the whole data set (top) or a subset with $\log_{10}(P/\mathrm{d}) < 1.8$ (bottom).

systems. Our results are summarized in Figs 8 and 9 which show the statistical agreement between the model populations and the observations.

The comparison between the observations and the entire model population shows that the two populations are compatible (at a distance of about 0.4σ) while the short-period systems lie at about 1.6–2.2σ, matching the numbers provided in Table 4 for M35. We see that this agreement does not vary significantly despite the wide range of tidal strength factors explored. This shows that main-sequence tides are not relevant to justify current observations of binary systems in the M35 cluster and that the choice of the initial distributions of period and eccentricity (that

depend in part on PMS tidal dissipation) has a much greater impact.

M35 is a young open cluster (150 Myr), while M67 is significantly older (4 Gyr) and is more likely to carry a tide signature. As shown in Fig. 9, the entire observed and model populations are compatible (at a distance lower than 1σ for both tide prescriptions). When focusing on circularizing systems at $\log_{10}(P/\mathrm{d}) < 1.8$, the model populations lie 1.9 and 1.6σ away from the observations when using unaltered BSE and MINT tides, respectively. When using the detailed implementation of Zahn's prescriptions with MINT, this agreement remains roughly constant and worsens only when multiplying the base tidal dissipation by more than 100. However, when the calculations are based on BSE simplified prescriptions, we observe an improvement of the agreement between observations
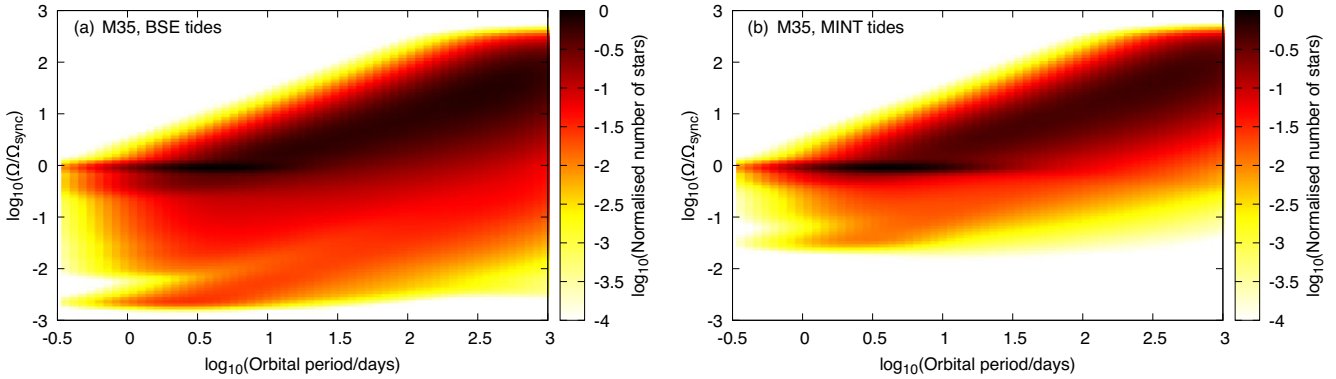
Figure 10. Angular frequency in units of the pseudo-synchronous angular frequency for M35 at age 150 Myr, evolved with BSE (a) or MINT (b) tides starting from the BSE rotation velocities prescribed by equation (1).

and model by $\sim 0.4\sigma$ when multiplying tidal coefficients by 30 to 100. While this improvement is noticeable only when focusing on low-period systems and not significant, it matches the works of Belczynski et al. (2008) and Geller, Hurley & Mathieu (2013) that obtained more realistic circularization distributions by multiplying BSE's convective damping by 50 to 100.

4 CAN SYNCHRONIZATION HELP DIFFERENTIATE TIDAL PRESCRIPTIONS?

From the study of $e - \log_{10}(P/\mathrm{d})$ distributions of a variety of clusters, it appears that circularization in stellar populations is dominated by the initial distribution of eccentricities and periods, preventing us from constraining tidal efficiency beyond the PMS and early-main-sequence phases. However, tides do not only circularize binary orbits, they also synchronize the stellar spins with the orbit over time. In a priori eccentric systems, tides act more efficiently where the distance between the stars is minimal, leading to a synchronization of spins with the orbit at periastron. The resulting angular frequency is called pseudo-synchronous (Hut 1981). We study the evolution of stellar spins in open clusters in search of a tide-dependent signature beyond the early main-sequence.

In this section we test BSE and MINT tidal prescriptions with Moe & di Stefano initial distributions focussing on the evolution of stellar rotational properties. As in Section 2.5.2, we consider four initial rotation settings: BSE's prescription from Hurley et al. (2000) given in equation (1), a very low equatorial velocity of $v_{\mathrm{rot}} = 10^{-4}$ km s^{-1}, initial breakup velocities or spin-orbit synchronous rotation. We focus here on the two clusters M35 and Tarantula, presented in detail in Section 3.

4.1 M35

We start with our fiducial example, M35, assuming an initial rotation profile matching the BSE prescription given in equation (1).

Fig. 10 presents the ratio of the stellar angular frequency to the pseudo-synchronous one, on a logarithmic scale for both tidal prescriptions. In each panel, the high-count diagonal feature across the plot is the signature of the initial rotation rate which is a function of mass only while the pseudo-synchronous rate is a decreasing function of the orbital period. Stars in short-period systems are spun up by tides while those in wider systems retain their initial low angular frequency. This change in behaviour happens at $\log_{10}(P/\mathrm{d})$ ~ 1.5 with both BSE and MINT tides. Tidal synchronization leads to

a higher stellar count near $\log_{10}(\Omega/\Omega_{\mathrm{sync}}) = 0$ for close-in systems. Such a feature can be seen in both model populations, but is more prominent when using the more efficient MINT tides. This spin-up process activates in close-enough systems owing to the highly non-linear dependence on R/a in equations (A2) and (A16). On the contrary, stars in wide systems evolve towards slow rotation at all configurations of initial rotation rates, even when they are initially set at breakup velocity on the ZAMS. Angular momentum losses through magnetic braking slow these stars in the first million years of their main-sequence evolution regardless of the tidal prescription used. This competition between magnetic braking and tides is at the origin of the spread seen in Figs 10 and 11, and repeating this experiment with other initial rotation prescriptions confirms this result, with a dichotomy between spun up stars in short-period systems and slowly rotating wide systems.

Fig. 11 shows the model populations computed using MINT tides for different initial rotation distributions. Setting a pseudo-synchronous angular frequency at the ZAMS, we would expect the ratio $\Omega/\Omega_{\mathrm{sync}}$ to remain constant if only tides act on these stars, but magnetic braking slows these stars and its competition with tides leads to short-period systems near synchronicity in the range $-0.2 < \log_{10}\Omega/\Omega_{\mathrm{sync}} < 0.2$, and wide systems rotating more slowly and distributed over the wider range $-1.5 < \log_{10}\Omega/\Omega_{\mathrm{sync}} < 0$. Signatures of magnetic braking are also found in the sample starting with $v_{\mathrm{rot}} = 10^{-4}$ km s^{-1}. While some stars spin up and reach synchronicity, about 80 per cent of them remain at very low rotation rates, especially in wider orbits where tidal spin up is immediately compensated by magnetic braking. Similarly, systems forming at breakup velocity are rapidly spun down by the combined effects of tides and magnetic braking so that most signatures of the original high rotation rate vanish during the early cluster evolution.

To quantify the effects of tides and their competition with magnetic braking, we focus on close systems in Fig. 11 splitting them into two bins. Retaining only close systems at $\log_{10}(P/\mathrm{d}) < 1.5$, we count the fraction of stars in the $-0.2 < \log_{10}(\Omega/\Omega_{\mathrm{sync}}) < 0.2$ range that we deem synchronized.

Fig. 12 shows the fraction of stars near pseudo-synchronicity as a function of the population age, for $\log_{10}(P/\mathrm{d}) < 1.5$. The age of M35 is estimated at 150 Myr (Meibom & Mathieu 2005). These results show that MINT tides synchronize stellar spins with the orbit faster and in more systems with respect to BSE tides, even when changing between slow, breakup or BSE initial rotation rates. This is the result of the higher efficiency of MINT equilibrium tides discussed in Section A1.1. On average, we find that MINT equilibrium tides predict 30 to
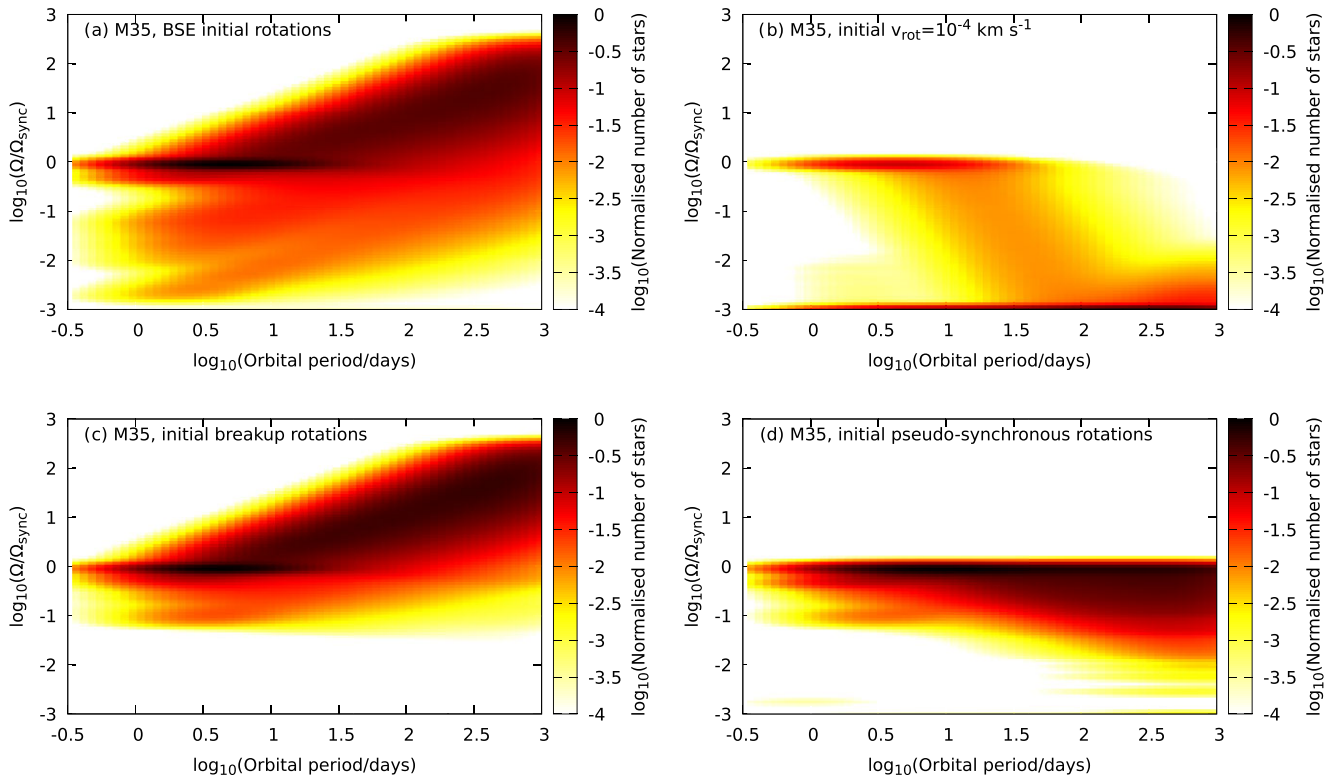
Figure 11. Angular frequency in units of the pseudo-synchronous angular frequency for M35 with MINT tides and Moe & di Stefano initial distribution, assuming four different initial rotation profiles: (a) BSE rotation prescription, (b) $v_{\rm rot} = 10^{-4}$ km s^{-1}, (c) breakup velocity, (d) pseudo-synchronous rotation.
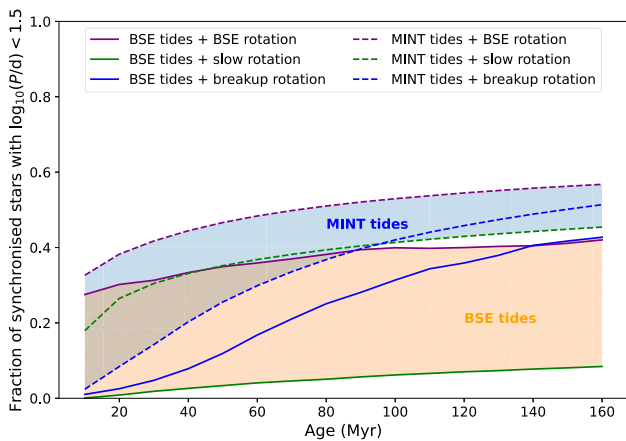

Figure 12. Fraction of M35 stars rotating at pseudo-synchronicity normalized to the total number of stars at $\log_{10}(P/{\rm d}) < 1.5$, assuming Moe & di Stefano initial distributions. The solid and dotted lines are obtained with BSE and MINT tides, respectively, for initial BSE rotation rates (purple), $v_{\rm rot} = 10^{-4}$ km s^{-1} (green), and initial breakup rotations (blue). The shaded areas show the domains of MINT (blue) and BSE (orange) tidal prescriptions.

50 per cent pseudo-synchronized stars, while their BSE counterparts predict on average one pseudo-synchronized star for each five that are not synchronized. This difference provides a simple criterion that can be tested through comprehensive surveys of clusters including solar-type binaries. Including orbital parameters to determine the exact pseudo-synchronous rotation period and individual stellar rotation periods would therefore allow us to quantify the relative efficiency of

tides and magnetic braking and favour a prescription. For instance, Meibom, Mathieu & Stassun (2006) use joint observations of the orbital and rotational parameters of M35 systems and find that two of the four close systems they characterize are rotating synchronously. Such a result seems to favour the MINT tidal prescription, but needs to be confirmed by more systems in M35 and other clusters containing late-type binaries.

4.2 Tarantula

We repeat the above experiment with the Tarantula cluster, whose population of young and massive O stars differs significantly from that of M35. Most importantly, as these stars have a thick radiative envelope, they harbour dynamical tides that follow the formalism laid out in Section A2 and angular momentum losses arise from stellar winds rather than magnetic braking. We use the wind mass-loss prescription of Schneider et al. (2018) that was derived from observations of the Tarantula cluster.

In Fig. 13, we present the rotation rates in units of the pseudo-synchronous rotation rate. As in Fig. 10, the diagonal feature at high periods is the signature of the initial rotation rate. Systems with $\log_{10}(P/{\rm d}) < 1.5$ have a relatively high fraction of pseudo-synchronized systems in the four cases shown here, that lies between 40 per cent for systems started at breakup and evolved with MINT tides and 60 per cent for systems started at BSE rotation rates with BSE tides.

Fig. 14 quantifies the evolution of this fraction of synchronized stars as a function of age. The Tarantula population formed between 1 and 7 Myr ago, with a peak of star formation 4 Myr ago. At such young ages, tides cannot be differentiated from synchronization
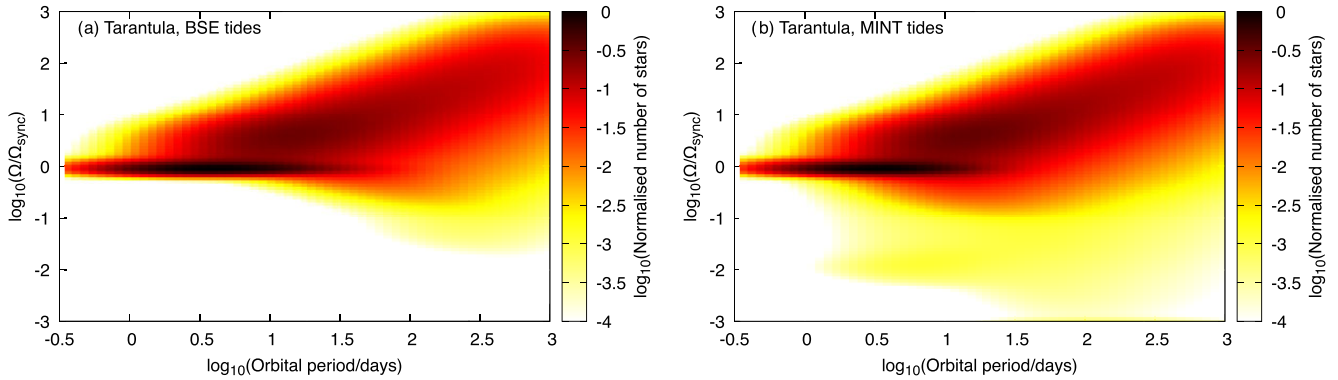
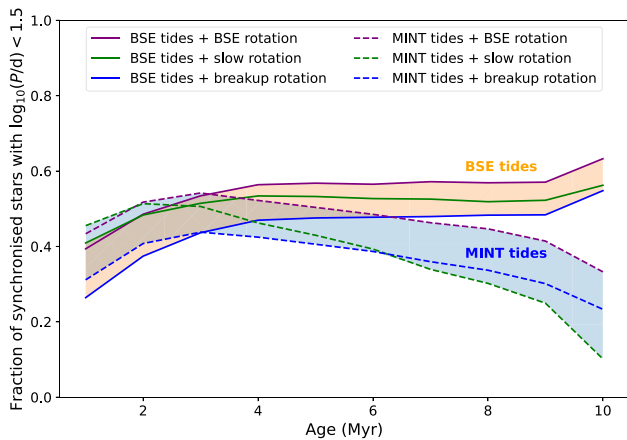**Figure 13.** As Fig. 10 for the Tarantula population.

Figure 14. As Fig. 12 for Tarantula.

processes, as both tidal prescriptions have similar efficiencies near the ZAMS. However, MINT dynamical tides become less efficient over time while BSE dynamical tides are not age-dependent. Winds cause a loss of angular momentum for which MINT dynamical tides cannot compensate after a certain age, so that some systems fall out of pseudo-synchronicity, and the fraction of pseudo-synchronous stars drops from ∼45 per cent to ∼25 per cent. On the contrary, the model populations evolved with BSE tides have a steady ∼50 per cent pseudo-synchronous stars. As with equilibrium tides, this difference induced by tidal prescriptions depends only slightly on the choice of initial rotation, the range covered using different prescriptions is highlighted by the shaded areas in Fig. 14. This would leave a detectable signature in a 10 Myr old Tarantula twin cluster, as BSE dynamical tides would predict as many pseudo-synchronized as non-synchronized systems while their MINT counterparts predict only one pseudo-synchronized system for every three that are not syn-chronized. Appropriate measurements of the orbital and rotational properties of close systems in older, massive-star open clusters can thus decide which prescription is more suitable for dynamical tides between BSE and MINT.

5 DISCUSSION

Our model populations show that circularization depends much more on the initial orbital parameter distribution than on the tidal efficiency on the main sequence (MS), even when using an ad hoc multiplicative

factor, establishing that MS tides are inefficient. The presence of a short-period low-eccentricity clump ($0.5 < \log_{10}(P/\mathrm{d}) < 1.3$, $e < 0.1$), surviving from the Moe & Di Stefano (2017) initial orbital parameter distribution, confirms that PMS interactions are crucial to describe the current eccentricity and period distributions of observed open clusters. Such a hypothesis was proposed by Zahn & Bouchet (1989) and recent theoretical developments match our conclusions. Terquem & Martin (2021) show, relying on the formalism of Terquem (2021), that equilibrium tides are very efficient on the PMS but inefficient on most of the MS. It is only when stars develop an extensive convective envelope upon reaching the very end of the MS or the subgiant phase (age $\gtrsim 10$ Gyr for a $1\,\mathrm{M}_\odot$ star) that their equilibrium tide efficiency increases to the same order of magnitude as on the PMS. Calculations invoking wave dissipation through resonance-locking mechanisms usually yield increased tidal circularization rates, which could lead to significant tides on the main sequence. This is however not seen, as works such as Zanazzi & Wu (2021) reach the same conclusion that MS dynamical tides contribute much less than PMS tides to circularization. An exhaustive implementation of these mechanisms over the whole parameter range is necessary for population synthesis which would offer a definitive answer.

The PMS tide efficiency is included in our calculations through the initial distributions, which we take from Moe & Di Stefano (2017). Further work by Moe & Kratter (2018) investigates the origin of this distribution, and concludes that most of the close binaries migrated to short periods during the PMS phase under the associated action of the Kozai–Lidov mechanism (from a very long-period triple), dynamical instability, and tidal friction. Together, these formation channels explain the large number of close binaries observed (highlighted by the low-eccentricity short-period clumping in our model populations). Our calculations also show that circular and eccentric systems coexist at intermediate periods (3–20 d). PMS migration explains this mixed population with inflated stars on the Hayashi track circularizing efficiently even at periods as long as a few weeks, and stars migrating later not circularizing fully. This situation would then remain generally the same throughout the MS. Investigating older populations, such as halo and field stars with ages about 10 Gyr included in Meibom & Mathieu (2005), would provide insights on late-MS tidal dissipation. Recent developments in asteroseismology and astrometry, ushered with the *TESS* and *Gaia* missions, offer unprecedented statistics on binary systems in the field that can yield crucial insights on tidal efficiency on and beyond the main sequence (Beck et al. 2023). However, such populations are not as homogeneous as stellar clusters and their initial conditions and

ages would raise numerous uncertainties on the population synthesis process.

Unfortunately, the relative inefficiency of MS tides renders the analysis of circularization and the $e - \log_{10}(P/\text{d})$ distribution a poor method of constraining tides in clusters. Defining a cut-off or circularization period from the observed orbital parameters is a complicated task (Meibom & Mathieu 2005) that might be irrelevant altogether. Zanazzi (2022) may offer a solution to this conundrum, by shifting the focus from circular to eccentric short-period systems. Based on the combined study of clusters presented here and Kepler eclipsing binaries, they divide the samples into two populations: nearly circular binaries whose periods extend higher than measured circularization periods and an envelope of eccentric systems at periods as low as ~3 d. These populations also appear in the Moe & Di Stefano (2017) initial distributions we use in this work. Through a fit similar to the one performed by Meibom & Mathieu (2005) to obtain circularization periods, but only applied to the most eccentric systems at each orbital period, they derive the envelope period. This indicator yields a statistically significant difference between young (<1 Gyr) and old clusters (>3 Gyr) and may carry the signature of MS equilibrium tides. Another tentative explanation has been offered by Bashi et al. (2023), which analysed 17 000 MS systems from the third *Gaia* data release, focussing on the eccentric systems as well. They find that the envelope period scales linearly with the stellar effective temperature rather than age, leading to a decreasing envelope period with increasing stellar masses. While they highlight needed observation advances, we contend population synthesis can offer theoretical insights into the temperature dependence of tidal dissipation. Studying the impact of various tidal mechanisms on the cut-off periods estimated on circular and eccentric systems by means of population synthesis codes will be the focus of future work.

In this work, we also propose the study of the rotational properties of cluster stars, as synchronization carries the signature of tidal efficiency well into the MS evolution of the stars in the system. We quantify this signature in terms of the fraction of near-synchronous stars at short periods, which varies with tidal efficiency and cluster age. This criterion can be tested observationally, by measuring both orbital parameters and individual stellar spins through the combination of spectroscopy and photometry. Early attempts at such an analysis include Giuricin, Mardirossian & Mezzetti (1984, and references therein) who find synchronization rates compatible with Zahn's theory. State-of-the-art population studies that rely on modern stellar physics will be a key tool to better constrain main-sequence tidal efficiency from surveys of rotational and orbital parameters. However, such surveys are rare and sparse (Meibom et al. 2006; Rebull et al. 2017), and need to be completed and extended to more clusters of main-sequence stars.

The angular momentum changes of each star, and thus the fractions of pseudo-synchronized rotators, are the result of the competition between equilibrium tides and magnetic braking in low-mass stars or between dynamical tides and stellar winds in massive stars. Both winds and magnetic braking tend to push stars out of synchronicity and explain why short-period systems can all be circularized but still not synchronized with the orbit. Investigating the magnetic braking and wind mass-loss prescriptions in the literature and their impact on the modelled fraction of stars rotating synchronously will also be important to establish the measurability of tidal efficiency, and the topic of future work.

The eccentricity-period distribution in open clusters is reminiscent of that of barium/CH/CEMP-s stars. These stars are in binary systems and present the same dichotomy between short-period circular systems and longer period eccentric systems that tidal interactions do not seem to explain (Jorissen et al. 1998, 2016). The key to barium stars can be tides acting during the red-giant phase. The calculations we present here apply to other stages of stellar evolution than the MS, and the inclusion of red giant stars in the MINT evolution algorithm along with the relevant tides will be at the core of upcoming work and is relevant to the study of numerous classes of stars. Beyond barium stars, tides affect the fraction of synchronized systems and thus the angular momentum budget available for Wolf–Rayet stars to form a soft-long gamma-ray burst. If dynamical tides cannot compensate for wind mass-loss in the late-MS phase and beyond, most massive stars will not evolve into a collapsar that can form a disc necessary to the burst (Izzard, Ramirez-Ruiz & Tout 2004a; Detmers et al. 2008). Efficient dynamical tides are also necessary to form chemically homogeneous stars that provide a channel to binary black holes in near-contact, low-metallicity massive binaries (Mandel & de Mink 2016), while the competition between tides and wind mass-loss affects the number of mergers predicted by this channel (de Mink & Mandel 2016). Both these applications require a thorough study at low metallicity including post-MS evolution.

6 CONCLUSIONS

To summarize, we investigated the circularization process in open clusters, in which two populations of binary systems coexist: circular systems with $P < 10$–20 d and eccentric systems with $P > 6$–10 d, with both circular and eccentric systems coexisting at intermediate periods in what appears to be a tidally driven transition period. To investigate the origin of this distribution, we implement and test detailed calculations of tidal dissipations for main-sequence stars. We compute the coefficients E and E_2 using Zahn's theory of equilibrium and dynamical tides, relying on extensive grids of MESA structures (covering $M = 0.1$–320 M$_\odot$ and $Z = 0$–0.02), and implement them in the BINARY_C stellar population code. With respect to the ubiquitous BSE prescriptions, the MINT implementation yields equilibrium tides three to six times more efficient and dynamical tides similar at the ZAMS that then drop several orders of magnitude with age. The impact on individual systems is significant. The maximum period for circular systems at $1 + 0.5$ M$_\odot$ is 6 or 15 d with BSE or MINT equilibrium tides, respectively, for a $50 + 25$ M$_\odot$ system it is 25 d or 7.2 d with BSE or MINT tides, respectively.

We then study $e - \log_{10}(P/\text{d})$ distributions of binary stars in open clusters over a wide range in age by modelling stellar populations with both BSE and MINT tidal prescriptions and initial distributions derived from bias-corrected observed properties (Moe & Di Stefano 2017). We assess the agreement between our model populations and orbital parameters measured for binary stars in eight open clusters through a 2D KS estimation. The statistical agreement is excellent for most clusters, and mostly independent of the tidal prescription used (both MINT and BSE tides typically lie within 0.3σ of each other). This is due to a concentration of systems around $\log_{10}(P/\text{d}) \sim 0.8$, $e = 0.05$, a direct consequence of the Moe & di Stefano distributions that tides do not modify over the main-sequence cluster evolution. This agreement does not change significantly even when multiplying tides by a constant factor between 0 and 1000, but changing the initial distributions to ones that do not include primordial short-period low-eccentricity systems degrades the agreement very significantly for all clusters. We conclude that main-sequence tides have a very limited impact on the statistical agreement between observations and model populations, which makes the comparison between synthetic and observed $e - \log_{10}(P/\text{d})$ diagrams an unsuitable way of constraining tidal prescriptions.

We then compute the synchronization of stellar spins with orbital periods and find that BSE and MINT tides efficiencies consistently yield different fractions of stars rotating at pseudo-synchronicity. In clusters of low-mass stars, MINT equilibrium tides are more efficient and lead to more synchronous rotators over time, while the situation is reversed in clusters of massive stars. In M35 for instance, we expect about 40 per cent of the stars to rotate near pseudo-synchronicity if MINT tides apply, while BSE tides would only yield 20 per cent of such stars. For a massive-star cluster such as Tarantula, the fraction of pseudo-synchronized O stars decreases with time as tides become less efficient and wind mass-loss removes angular momentum from the stars. While the synchronized rotator fraction is similar for both BSE and MINT tides in Tarantula at its current age, a similar population at age 10 Myr would have three times fewer synchronized stars if MINT tides apply in lieu of BSE tides. These effects are significant and yield a workable criterion on the fraction of stars rotating at pseudo-synchronicity that could be tested through combined spectroscopic and photometric observations of the orbital parameters of the systems and the individual stellar spins.

SOFTWARE

We acknowledge the use of the following software:

(i) The MESA stellar evolution code (http://mesa.sourceforge.net/) and Section 2.2.

(ii) The BINARY_C stellar population synthesis code version 2.2.1, commit SHA 679b741fe, (http://personal.ph.surrey.ac.uk/~ri0005/binary_c.html) and Section 2.3.

(iii) The BINARY_C-PYTHON software package (Hendriks & Izzard 2023).

(iv) The Python implementation of the two-dimensional two-sample KS estimator, by Zhaozhou Li (https://github.com/syrte/ndtest).

(v) The GNU Scientific Library (Galassi 2018).

ACKNOWLEDGEMENTS

DATA AVAILABILITY

The data underlying this article have been generated using free software and will be shared upon request to the corresponding author.

REFERENCES

Almeida L. A. et al., 2017, A&A, 598, A84
Andronov N., Pinsonneault M., Sills A., 2003, ApJ, 582, 358
Barker A. J., 2020, MNRAS, 498, 2270
Barker A. J., 2021, Tidal dissipation in stars and predictions for planetary orbital decay, Zenodo, available at: https://doi.org/10.5281/zenodo.5636302
Barker A. J., 2022, ApJ, 927, L36
Barker A. J., Astoul A. A. V., 2021, MNRAS, 506, L69
Bashi D., Mazeh T., Faigler S., 2023, MNRAS, 522, 1184
Beck P., Grossmann D., Steinwender L., Schimak L. S., Muntean N., Mathur S., Garcia R., Pinsonneault M., 2023, preprint (arXiv:2307.10812)
Belczynski K., Kalogera V., Rasio F. A., Taam R. E., Zezas A., Bulik T., Maccarone T. J., Ivanova N., 2008, ApJS, 174, 223
Bragaglia A. et al., 2001, AJ, 121, 327
Burkart J., Quataert E., Arras P., Weinberg N. N., 2012, MNRAS, 421, 983
Choudhury S., Subramaniam A., Piatti A. E., 2015, AJ, 149, 52
Christensen-Dalsgaard J., Monteiro M. J. P. F. G., Rempel M., Thompson M. J., 2011, MNRAS, 414, 1158
Claret A., Cunha N. C. S., 1997, A&A, 318, 187
De Marco O., Izzard R. G., 2017, Publ. Astron. Soc. Aust., 34, e001
de Mink S. E., Mandel I., 2016, MNRAS, 460, 3545
Detmers R. G., Langer N., Podsiadlowski P., Izzard R. G., 2008, A&A, 484, 831
Duquennoy A., Mayor M., 1991, A&A, 500, 337
Fasano G., Franceschini A., 1987, MNRAS, 225, 155
Galassi M. e. a., 2018, GNU Scientific Library Reference Manual, available at: https://www.gnu.org/software/gsl/
Geller A. M., Mathieu R. D., 2012, AJ, 144, 54
Geller A. M., Mathieu R. D., Harris H. C., McClure R. D., 2009, AJ, 137, 3743
Geller A. M., Hurley J. R., Mathieu R. D., 2013, AJ, 145, 8
Geller A. M., Mathieu R. D., Latham D. W., Pollack M., Torres G., Leiner E. M., 2021, AJ, 161, 190
Giuricin G., Mardirossian F., Mezzetti M., 1984, A&A, 141, 227
Goldreich P., Keeley D. A., 1977, ApJ, 211, 934
Goldreich P., Nicholson P. D., 1977, Icarus, 30, 301
Grevesse N., Sauval A. J., 1998, Space Sci. Rev., 85, 161
Griffin R. F., Gunn J. E., 1978, AJ, 83, 1114
Griffin R. F., Gunn J. E., 1981, AJ, 86, 588
Griffin R. F., Mayor M., Gunn J. E., 1982, A&A, 106, 221
Griffin R. F., Gunn J. E., Zimmerman B. A., Griffin R. E. M., 1985, AJ, 90, 609
Hendriks D., Izzard R., 2023, J. Open Source Softw., 8, 4642
Hole K. T., Geller A. M., Mathieu R. D., Platais I., Meibom S., Latham D. W., 2009, AJ, 138, 159
Hurley J. R., Pols O. R., Tout C. A., 2000, MNRAS, 315, 543
Hurley J. R., Tout C. A., Pols O. R., 2002, MNRAS, 329, 897
Hut P., 1981, A&A, 99, 126
Izzard R. G., Ramirez-Ruiz E., Tout C. A., 2004a, MNRAS, 348, 1215
Izzard R. G., Tout C. A., Karakas A. I., Pols O. R., 2004b, MNRAS, 350, 407
Izzard R. G., Dray L. M., Karakas A. I., Lugaro M., Tout C. A., 2006, A&A, 460, 565
Izzard R. G., Glebbeek E., Stancliffe R. J., Pols O. R., 2009, A&A, 508, 1359
Izzard R. G., Preece H., Jofre P., Halabi G. M., Masseron T., Tout C. A., 2018, MNRAS, 473, 2984
Jorissen A., Van Eck S., Mayor M., Udry S., 1998, A&A, 332, 877
Jorissen A. et al., 2016, A&A, 586, A158
Kroupa P., 2001, MNRAS, 322, 231
Lang K. R., 1992, Astrophysical Data I. Planets and Stars. Springer-Verlag, Berlin, Heidelberg, New York
Langer N., El Eid M. F., Fricke K. J., 1985, A&A, 145, 179
Leiner E. M., Mathieu R. D., Gosnell N. M., Geller A. M., 2015, AJ, 150, 10
Ma L., Fuller J., 2021, ApJ, 918, 16
Mandel I., de Mink S. E., 2016, MNRAS, 458, 2634
Mathieu R. D., Meibom S., Dolan C. J., 2004, ApJ, 602, L121
Meibom S., Mathieu R. D., 2005, ApJ, 620, 970
Meibom S., Mathieu R. D., Stassun K. G., 2006, ApJ, 653, 621
Mermilliod J. C., Mayor M., 1999, A&A, 352, 479
Mermilliod J.-C., Weis E. W., Duquennoy A., Mayor M., 1990, A&A, 235, 114
Mermilliod J. C., Bratschi P., Mayor M., 1997, A&A, 320, 74
Mermilliod J. C., Rosvick J. M., Duquennoy A., Mayor M., 1992, A&A, 265, 513

Milliman K. E., Mathieu R. D., Geller A. M., Gosnell N. M., Meibom S., Platais I., 2014, AJ, 148, 38

Moe M., Di Stefano R., 2017, ApJS, 230, 15

Moe M., Kratter K. M., 2018, ApJ, 854, 44

Nine A. C., Milliman K. E., Mathieu R. D., Geller A. M., Leiner E. M., Platais I., Tofflemire B. M., 2020, AJ, 160, 169

Ogilvie G. I., 2014, ARA&A, 52, 171

Ogilvie G. I., Lin D. N. C., 2007, ApJ, 661, 1180

Paxton B., Bildsten L., Dotter A., Herwig F., Lesaffre P., Timmes F., 2011, ApJS, 192, 3

Paxton B. et al., 2013, ApJS, 208, 4

Paxton B. et al., 2015, ApJS, 220, 15

Paxton B. et al., 2018, ApJS, 234, 34

Paxton B. et al., 2019, ApJS, 243, 10

Peacock J. A., 1983, MNRAS, 202, 615

Polfliet R., Smeyers P., 1990, A&A, 237, 110

Press W. H., Teukolsky S. A., 1988, Comput. Phys., 2, 74

Qin Y., Fragos T., Meynet G., Andrews J., Sørensen M., Song H. F., 2018, A&A, 616, A28

Raghavan D. et al., 2010, ApJS, 190, 1

Rasio F. A., Tout C. A., Lubow S. H., Livio M., 1996, ApJ, 470, 1187

Rebull L. M., Stauffer J. R., Hillenbrand L. A., Cody A. M., Bouvier J., Soderblom D. R., Pinsonneault M., Hebb L., 2017, ApJ, 839, 92

Rieutord M., 1992, A&A, 259, 581

Rieutord M., Zahn J.-P., 1997, ApJ, 474, 760

Sana H. et al., 2012, Science, 337, 444

Savonije G. J., Papaloizou J. C. B., 1984, MNRAS, 207, 685

Schneider F. R. N. et al., 2018, Science, 359, 69

Serenelli A. M., Basu S., 2010, ApJ, 719, 865

Siess L., Izzard R. G., Davis P. J., Deschamps R., 2013, A&A, 550, A100

Stephens M. A., 1992, Introduction to Kolmogorov (1933) On the Empirical Determination of a Distribution. Springer, New York, p. 93

Tassoul J.-L., 1987, ApJ, 322, 856

Tassoul J.-L., 1988, ApJ, 324, L71

Terquem C., 2021, MNRAS, 503, 5789

Terquem C., Martin S., 2021, MNRAS, 507, 4165

Terquem C., Papaloizou J. C. B., Nelson R. P., Lin D. N. C., 1998, ApJ, 502, 788

Tsamis Y. G., Péquignot D., 2005, MNRAS, 364, 687

Vidal J., Barker A. J., 2020, ApJ, 888, L31

Wei X., 2022, A&A, 664, A10

Willems B., van Hoolst T., Smeyers P., 2003, A&A, 397, 973

Witte M. G., Savonije G. J., 2002, A&A, 386, 222

Yoon S. C., Woosley S. E., Langer N., 2010, ApJ, 725, 940

Zahn J. P., 1966, Ann. Astrophys., 29, 489

Zahn J. P., 1970, A&A, 4, 452

Zahn J. P., 1975, A&A, 41, 329

Zahn J. P., 1977, A&A, 500, 121

Zahn J. P., 1989, A&A, 220, 112

Zahn J. P., 2008, in Goupil M. J., Zahn J. P.eds, EAS Publ. Ser. Vol. 29, Tidal Effects in Stars, Planets and Disks. Cambridge Univ. Press, Cambridge, p. 67

Zahn J. P., Bouchet L., 1989, A&A, 223, 112

Zanazzi J. J., 2022, ApJ, 929, L27

Zanazzi J. J., Wu Y., 2021, AJ, 161, 263

SUPPORTING INFORMATION

Supplementary data are available at *MNRAS* online.

appendices.pdf

Please note: Oxford University Press is not responsible for the content or functionality of any supporting materials supplied by the authors. Any queries (other than missing material) should be directed to the corresponding author for the article.

APPENDIX A: MATHEMATICAL FORMALISM

The impact of tides on orbital parameters is usually expressed in terms of synchronization and circularization time-scales. The formalism in this section is a summary of that of Zahn (1977, 1989) Hut (1981), and Siess et al. (2013). All equations presented in this section use masses, radii, and luminosities in Solar units unless otherwise specified. The dominating tides, and the associated set of equations governing them, depend on whether the envelope of the star is convective or radiative.

A1 Equilibrium tide: convective damping

A1.1 Circularization and synchronization time-scales

In stars with a convective outer envelope, or fully convective stars, we use the formalism of Zahn (1989),

$$\frac{1}{\tau_{\text{circ}}} = \frac{|\dot{e}|}{e} = 21 \frac{\lambda_{10}}{\tau_{\text{conv}}} \tilde{q} (1 + \tilde{q}) \left(\frac{R}{a} \right)^8, \tag{A1}$$

and

$$\frac{1}{\tau_{\text{sync}}} = \frac{|\dot{\Omega}|}{\Omega - \omega} = 6 \frac{\lambda_{22}}{\tau_{\text{conv}}} \tilde{q}^2 \frac{M R^2}{I} \left(\frac{R}{a} \right)^6. \tag{A2}$$

The overdot marks the time derivative, a and e are the semimajor axis and eccentricity of the binary orbit, $\tilde{q}$ is the ratio of the companion mass to the mass of the star under consideration, and ω is the orbit angular velocity. M, R, and Ω are the mass, radius, and angular frequency of the star under consideration, respectively, while I is its momentum of inertia. Finally, the convective turnover time τ_{conv} is defined by Hurley et al. (2002) as

$$\tau_{\text{conv}} = 0.4311 \left[\frac{M_{\text{env}} R_{\text{env}} \left(R - \frac{1}{2} R_{\text{env}} \right)}{3L} \right]^{1/3} \text{yr}, \tag{A3}$$

where L is in turn the stellar luminosity, M_{env} the mass of the convective envelope, and R_{env} the depth of the core-envelope boundary.

Note that this definition of τ_{conv} is essentially similar to that of Zahn (1977) but the convective turnover time is computed assuming a typical convective element in the centre of the convective envelope rather than at its base.

We present here the derivation of the λ_{lm} coefficients, where the indices $(l, m) = (0, 1)$ and $(l, m) = (2, 2)$ correspond to the spherical harmonics used for the expansion of the tide-generating potential (Zahn 1977; Polfliet & Smeyers 1990) for circularization and synchronization, respectively. These coefficients are defined as

$$\lambda_{lm} = 0.8725 \left(\alpha' \right)^{4/3} E^{2/3} \times \mathcal{S}, \tag{A4}$$

where α' is related to the mixing length α_{MLT} through $\alpha' = 0.762 \alpha_{\text{MLT}}$, the coefficient E (not to be confused with E_2) depends on the stellar structure at the core-envelope interface, and $\mathcal{S}$ includes dissipation via integrals on the stellar structure. We now detail the E and $\mathcal{S}$ terms.

A1.2 The E *coefficient*

The structure parameter E is defined as

$$E = \rho_{\text{b}} \frac{4\pi R^3}{M} \left(\frac{H_{P,\text{b}} R}{r_{\text{b}}^2} \frac{m_{\text{b}}}{M} \right), \tag{A5}$$

where H_P is the pressure scale height and the index b denotes the base of the convective envelope. Zahn (1989) provides the value $E =$
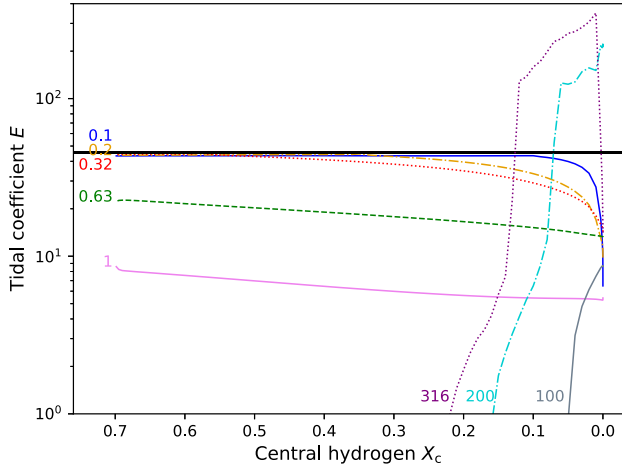
Figure A1. The E coefficient (equation (A5)) for a selection of stellar masses (indicated at the left or bottom of the plot), as a function of the central hydrogen mass fraction which is a proxy of age along the main sequence. The horizontal black line indicates the reference for a fully convective star from Zahn (1989).
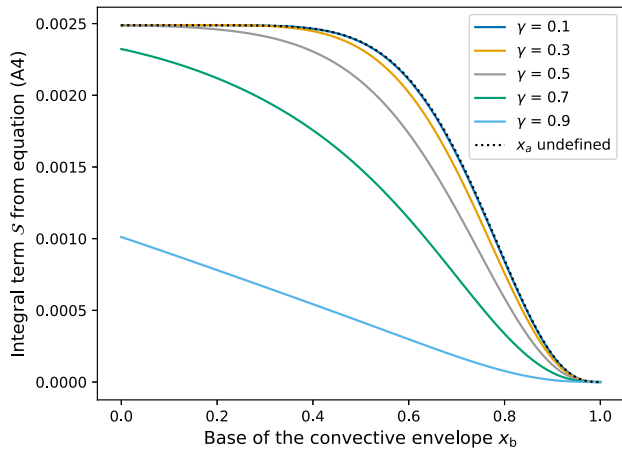

Figure A2. $\mathcal{S}$ from equation (A9) as a function of x_b for various values of γ, defined by $x_a = x_b + \gamma(1 - x_b)$. When $\gamma \to 0$, x_a becomes undefined and the corresponding $\mathcal{S}$ is marked by the dotted black line.

45.48 as a maximum only reached in fully convective stars. Fig. A1 shows E computed from our MESA models for a selection of masses (indicated on the left or bottom of the plot). The solid black line is Zahn's value which agrees with our early-main-sequence low-mass stars that are fully convective. We also find that very massive stars, $M > 90\,\mathrm{M_\odot}$, can have high E coefficients making equilibrium tides efficient as massive stars develop an extensive surface convection zone towards the end of the main sequence. We note that in these stars, E is larger than the maximum value of Zahn (1989). In his analysis of polytropes, Zahn focused on low-mass main-sequence and red giant stars, and did not consider such massive, inflated main-sequence stars.

Claret & Cunha (1997) provide the prescription

$$E = \frac{M_{\mathrm{env}}}{M} \times \left[\int_{x_b}^{1} \left(\frac{2(1-x)}{5x} \right)^{3/2} x^2 \mathrm{d}x \right]^{-1}, \qquad (A6)$$
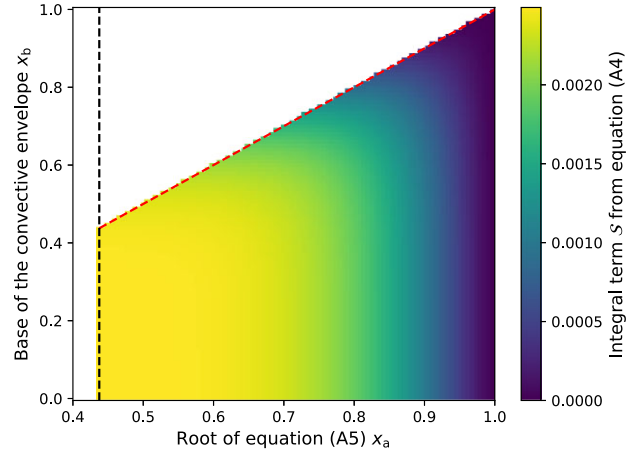
Figure A3. $\mathcal{S}$ from equation (A9) as a function of x_b and x_a. x_a left of the black line ($x_a = 7/16$) or above the red line ($x_a = x_b$) are not physical.
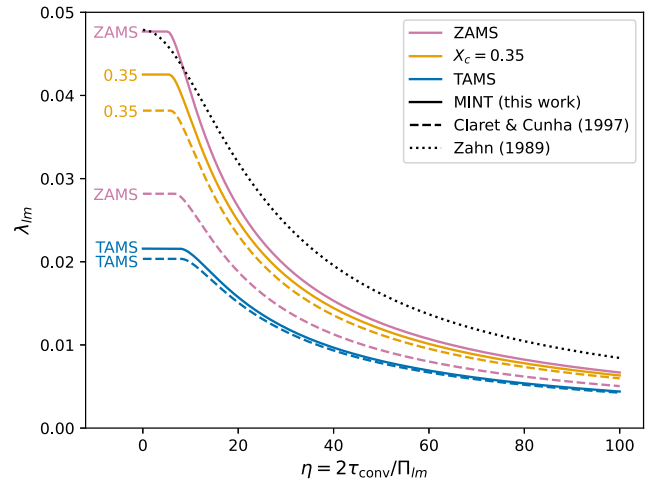

Figure A4. Comparison between λ_{lm} obtained from MINT (solid lines), Claret & Cunha (1997, dashed lines), and Zahn (1989, dotted line) for a $0.32\,M_\odot$ star at the ZAMS (pink), halfway through the MS (orange) and at the TAMS (blue). The Zahn (1989) prescription is independent of age.
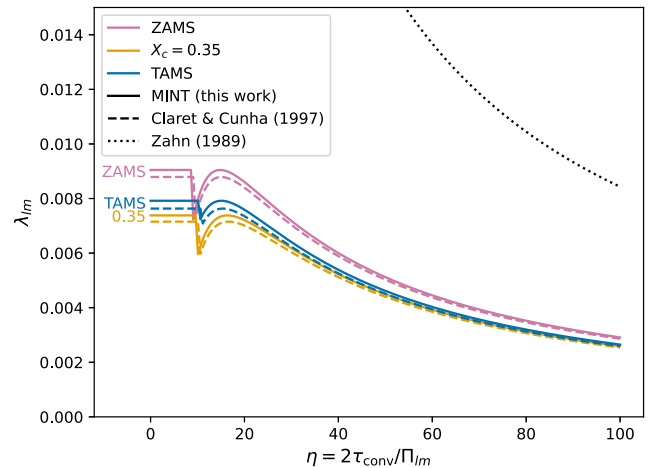

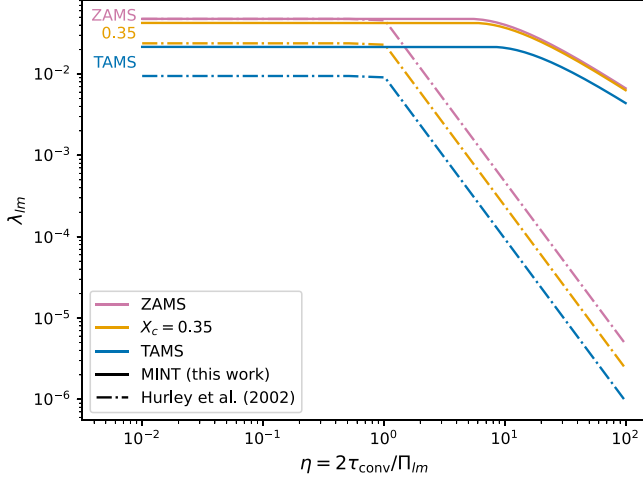**Figure A5.** As Fig. A4 for a $1\,M_\odot$ star.

Figure A6. Comparison between λ_{lm} obtained from MINT (solid lines) and BSE (dash–dotted lines) for a $0.32M_\odot$ star at the ZAMS (pink), halfway through the MS (orange) and at the TAMS (blue). Both axes are in logarithmic scale.
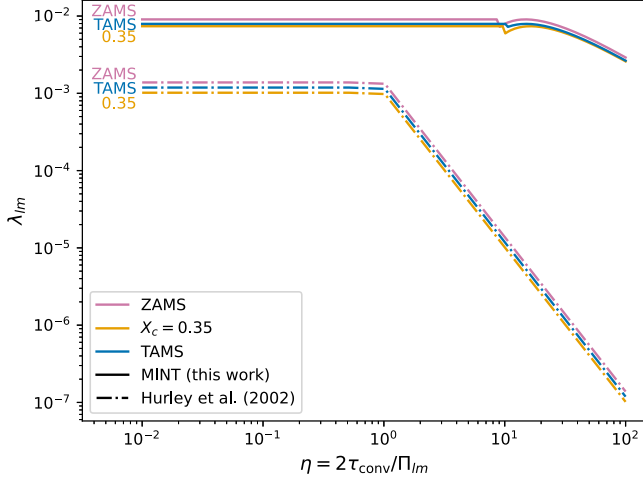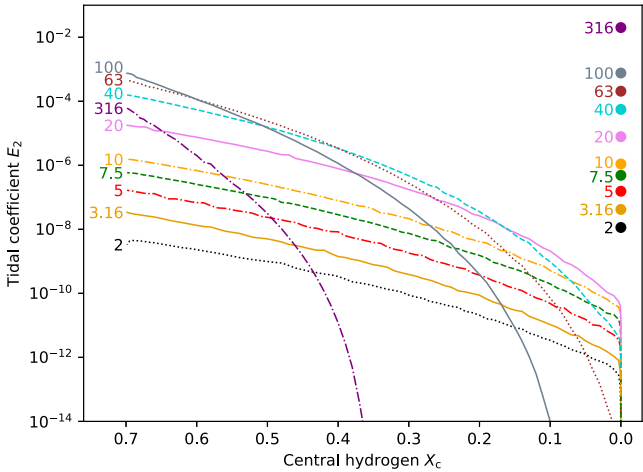

Figure A7. As Fig. A6 for a $1M_\odot$ star.

Figure A8. The E_2 coefficient (equation (A18)) for a selection of stellar masses (indicated on the left of the plot), as a function of the central hydrogen mass fraction at $Z = 0.02$. The dots in the upper right corner give the age- and metallicity-independent value from BSE, based on a fit of Zahn (1975).
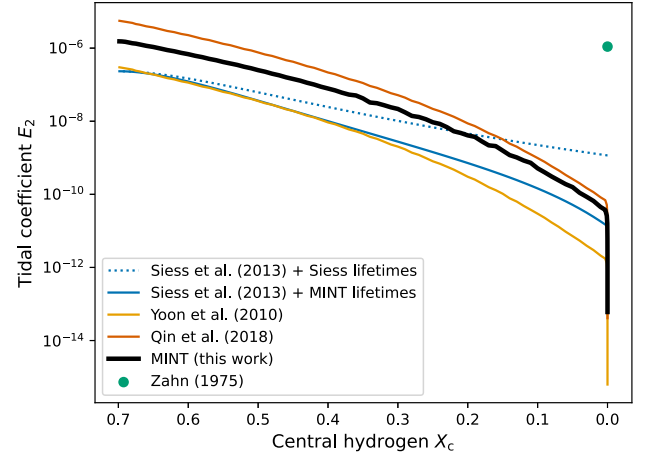

Figure A9. Comparison between coefficients E_2 for a $10M_\odot$ star. Colours mark the various prescriptions. Two calculations using Siess's prescriptions are presented (see the main text), while the Zahn prescription yields a constant value shown as a dot in the top-right corner.

where M_{env}/M is the relative mass of the convective envelope and $x = r/R$ is the relative radius throughout the star. Using this prescription will allow for comparison with our values of λ_{lm} in paragraph A1.4.

A1.3 The integrals underlying $\mathcal{S}$

The $\mathcal{S}$ term is equation (A4) quantifies the tidal efficiency through viscous dissipation in the convective envelope. For the first time in a population code, we implement the derivation of Zahn (1989) where the viscous dissipation depends on the ratio between the tidal period

$$\Pi_{lm} = \frac{2\pi}{|l\omega - m\Omega|}, \tag{A7}$$

and the convective turnover time τ_{conv} (equation (A3)).

If $\Pi_{lm} \geq 2\tau_{\mathrm{conv}}$ throughout the convective envelope, λ_{lm} depends on the stellar structure through

$$\mathcal{S} = \int_{x_{\mathrm{b}}}^1 x^{22/3}(1-x)^2 \mathrm{d}x, \tag{A8}$$

where $x = r/R$ is the reduced radius. Note that λ_{lm} is, in this case, the same for all indices l and m, thus for both circularization and synchronization.

If the tidal and convective turnover time-scales satisfy $\Pi_{lm} = 2\tau_{\mathrm{conv}}$ at a depth x_a in the convective envelope, the integral in equation (A8) splits into two terms, so that

$$\mathcal{S} = \int_{x_{\mathrm{a}}}^1 x^{22/3}(1-x)^2 \mathrm{d}x + x_{\mathrm{a}}^{7/6}(1-x_{\mathrm{a}})^{3/2} \int_{x_{\mathrm{b}}}^{x_{\mathrm{a}}} x^{37/6}(1-x)^{1/2} \mathrm{d}x. \tag{A9}$$

The first integral accounts for the viscous dissipation as in equation (A8) where $\Pi_{lm} > 2\tau_{\mathrm{conv}}$. Where this criterion is not valid, at $x_{\mathrm{b}} < x < x_{\mathrm{a}}$, convective cells cannot travel their expected mean free path before a reversal of the tidal excitation, which leads to a lower viscous dissipation that is accounted for by the second integral in $\mathcal{S}$ (Zahn 1989). The dependence on the tidal period, and therefore the indices l and m, is included in the integration limit x_a. The existence and numerical value of x_a is given by the roots of the equation

$$x_{\mathrm{a}}^{7/6}(1-x_{\mathrm{a}})^{3/2} = \left(\frac{5}{2}\right)^{3/2} (\alpha')^{-2/3} E^{-1/3} \frac{\Pi_{lm}}{2\tau_{\mathrm{conv}}}. \tag{A10}$$

The left-hand side of equation (A10) describes a bell-shaped function of x_a that reaches its maximum, $c \sim 0.16$, at $x_a = 7/16$. The equation has at most two roots, for the integral in equation (A4) we only retain the larger root if it is indeed inside the convective envelope (that is, $x_a > 7/16$ and $x_a > x_b$). We thus find that such a root exists if

$$\frac{\Pi_{lm}}{\tau_{\mathrm{conv}}} \leq 2c \left(\frac{2}{5}\right)^{3/2} (\alpha')^{2/3} E^{1/3}. \tag{A11}$$

We compute $\mathcal{S}$ from equation (A9). Both integrals in $\mathcal{S}$ have formal mathematical solutions that rely on the hypergeometric function $_2F_1$,

$$\int_{x_{\min}}^{x_{\max}} x^a (1-x)^b \mathrm{d}x = \left[\frac{x^{a+1}}{a+1} {}_2F_1(a+1, -b; a+2; x)\right]_{x_{\min}}^{x_{\max}}. \tag{A12}$$

In BINARY_C, we compute the integrals numerically using the GNU Scientific Library (GSL, Galassi 2018) and they agree with the formal expression within numerical precision.

Fig. A2 shows $\mathcal{S}$ at various convective interfaces x_b and the critical depths x_a. In this figure, $x_a = x_b + \gamma(1 - x_b)$, where γ is a constant between 0 and 1 that marks the limits and relative contributions of the integrals in equation (A9). γ tends to 1 when the tidal period is shorter than twice the convective turnover time everywhere in the star, leading to $\lambda_{lm} = 0$, while $\gamma = 0$ corresponds to tidal periods longer than twice the turnover time anywhere in the star, in which case x_a is formally undefined and equation (A9) simplifies into equation (A8). We find that $\mathcal{S} \rightarrow 0$ and thus that $\lambda_{lm} \rightarrow 0$ when the convective envelope is very thin ($x_b \rightarrow 1$) or if the tidal period is comparable with the convective turnover time throughout the envelope ($x_a \rightarrow 1$). The integral from x_b to 1 dominates $\mathcal{S}$, as the integral from x_a to x_b accounts for a reduced viscosity and thus contributes less to the tidal torque. Finally, the entire range of $\mathcal{S}$ values over the accessible x_a and x_b is shown in Fig. A3.

A1.4 Putting equilibrium tides together

We have now detailed both E and $\mathcal{S}$ and can use them in equation (A4). The coefficients λ_{lm} depend on the ratio $\eta = 2\tau_{\mathrm{conv}}/\Pi_{lm}$ through the limits of the integrals underlying $\mathcal{S}$.

In order to compare the MINT derivation with the literature, we use E from Claret & Cunha (1997) (equation (A6)) and the fitting formula from Zahn (1989):

$$\lambda_{lm} = 0.019 \, \alpha_{\mathrm{MLT}}^{4/3} \sqrt{\frac{320}{320 + \eta^2}}. \tag{A13}$$

Figs A4 and A5 present the three calculations at $Z = 0.02$, for 0.32 and $1\,\mathrm{M_\odot}$, respectively. Each of these plots presents λ_{lm} at the beginning, the end, and halfway through the main sequence ($X_c = 0.35$). As shown in Fig. A4, we find a good agreement between our prescription and Zahn's fit for $M = 0.32\,\mathrm{M_\odot}$ at the ZAMS as the star is fully convective there. The agreement deteriorates at later ages as a radiative core expands in the star. On the contrary, the match between Claret & Cunha's prescription improves as the star ages and becomes more radiative. Closer inspection of equation (A6) provides an explanation. If the star is fully convective, $M_{\mathrm{env}}/M \rightarrow 1$ and $x_b \rightarrow 0$, thus yielding $E = 20.13$. This is much smaller than both Zahn's and MINT's E. If the star is not fully convective, Zahn's prescription becomes irrelevant, while Claret & Cunha's prescription relying on the envelope mass yields a much better agreement with

our full calculation. This is visible in Fig. A5 for a $1\,\mathrm{M_\odot}$ star which features a radiative core throughout its main-sequence evolution.

In BSE prescriptions, equations (A1) and (A2) are cast in the slightly different form given by Rasio et al. (1996) to depend on the parameter $(k/T)_c$. This parameter encompasses the dependence of the circularization and synchronization time-scales on the ratio between convective turnover time and tidal period in the same way as λ_{22} and λ_{01}. Comparing the BSE and MINT mathematical derivations yields the equivalence

$$\lambda_{lm} = \frac{\tau_{\mathrm{conv}}}{2} \left(\frac{k}{T}\right)_c = \frac{1}{21} \frac{M_{\mathrm{env}}}{M} \min\left(1, \eta^2\right), \tag{A14}$$

where $\eta = 2\tau_{\mathrm{conv}}/\Pi_{lm}$ with $(l, m) = (2, 2)$ for synchronization and $(l, m) = (0, 1)$ for circularization, and τ_{conv} is given by equation (A3).

We present in Figs A6 and A7 the comparison between our derivation and the equivalent BSE λ_{lm} obtained through equation (A14). These plots are in logarithmic scale to emphasize the asymptotic behaviour of the coefficient at high and low η ratios. We see that BSE and MINT calculations agree at low η for the fully convective $M = 0.32\,\mathrm{M_\odot}$ model (Fig. A6), and diverge when a radiative core builds up. For the $M = 1\,\mathrm{M_\odot}$ model (Fig. A7), the disagreement reaches one order of magnitude and changes only slightly throughout the main-sequence evolution, as the core properties are not changed dramatically. This difference is intrinsic to the prescription used in Hurley et al. (2002) that scales linearly with the radiative core mass, while our estimate also takes the pressure scale height and core radius into account. We find that our MINT equilibrium tide prescriptions yield significantly higher λ_{lm} and thus faster circularization and synchronization.

The behaviour at large η displayed in Figs A6 and A7 is striking. The sharp drop in the BSE calculation does not match the MINT asymptotic slower decrease, the MINT λ_{lm} is larger than BSE's by several orders of magnitude. Tidal time-scales derived from the MINT prescription are shorter than BSE's by the same ratio. This difference can be traced to the prescription used for the viscosity when the convective turnover time and the tidal period are comparable. As the tidal period becomes larger than twice the convective turnover time ($\eta > 1$), convective cells cannot travel their expected mean free path before a reversal of the tidal excitation. This results in a drop in dissipation at high η that is parametrized either by multiplying the viscosity by a factor $1/\eta$ (Zahn 1966) or by a factor $1/\eta^2$ (Goldreich & Keeley 1977). Our derivation relies on the Zahn scaling which yields a matching -1 slope at high η, while BSE relies on the Goldreich & Keeley model through the $\min(1, \eta^2)$ factor in equation (A14) leading to the steeper -2 slope in Figs A6 and A7. In conclusion, our derivation of the equilibrium tide coefficients yields more efficient tides over both the mass and tidal period range. This is confirmed in Section 2.5.

A2 Dynamical tide: radiative damping

A2.1 Circularization and synchronization time-scales

In stars with a radiative envelope, the circularization and synchronization time-scales τ_{circ} and τ_{sync} are given by Zahn (1975, 1977):

$$\frac{1}{\tau_{\mathrm{circ}}} = \frac{|\dot{e}|}{e} = \frac{21}{2} \left(\frac{GM}{R^3}\right)^{1/2} \tilde{q}(1 + \tilde{q})^{11/6} E_2 \left(\frac{R}{a}\right)^{21/2}, \tag{A15}$$

and

$$\frac{1}{\tau_{\text{sync}}} = \frac{|\dot{\Omega}|}{\Omega - \omega} = 5 \left(2^{5/3}\right) \left(\frac{GM}{R^3}\right)^{1/2} \tilde{q}^2 \left(1 + \tilde{q}\right)^{5/6}$$
$$\times \frac{MR^2}{I} E_2 \left(\frac{R}{a}\right)^{17/2}, \tag{A16}$$

where most parameters follow the definitions given in equations (A1) and (A2). The key parameter is the remaining quantity E_2 (not to be confused with E) that depends on integrals of the stellar structure.

A2.2 The coefficient E_2

In the BSE implementation, E_2 is related to the stellar mass M through a fit to data provided by Zahn (1975)

$$E_2 = 1.592 \times 10^{-9} M^{2.84}. \tag{A17}$$

Most notably, this relation is age- and metallicity-independent. There have been several attempts at including the age-dependent core recession in the calculation of E_2, developed by Zahn (1977), Claret & Cunha (1997), and Siess et al. (2013). This latter work provides an attempt at computing E_2 as a function of mass, age, and metallicity. Our detailed derivation follows theirs which we summarize here.

$$E_2 = \gamma_2 \frac{\rho_b R^3}{M} \left[\frac{R}{g_s} \frac{d}{dx} \left(\frac{-gB}{x^2}\right)_b\right]^{-1/3} (H_2)^2 \tag{A18}$$

where the index b labels the convective core boundary and s the stellar surface, x is the relative radius, and g the local gravity. The constant γ_2 is

$$\gamma_2 = \frac{3^{8/3} \left[\Gamma(4/3)\right]^2}{5 \cdot 6^{4/3}} \sim 0.27384..., \tag{A19}$$

and B is defined from stellar structure quantities through

$$B = \frac{d}{dr} \ln \rho - \frac{1}{\Gamma_1} \frac{d}{dr} \ln P = \frac{\delta}{H_P} \left(\nabla - \nabla_{\text{ad}} - \frac{\psi}{\delta} \nabla_\mu\right). \tag{A20}$$

B is related to the Brunt–Väisälä frequency N through $N^2 = -gB$. The Brunt–Väisälä frequency is known to vary sharply at the interface between convective and radiative zones in upper main-sequence stars. Assessing the exact location of the core boundary is thus key for the calculation of E_2.

The last term remaining in the calculation of E_2 is H_2, defined as

$$H_2 = \frac{1}{X(x_b)Y(1)} \int_0^{x_b} X \left[\frac{d^2 Y}{dx^2} - \frac{6Y}{x^2}\right] dx, \tag{A21}$$

where X and Y are the solutions of the differential equations

$$\frac{d^2 X}{dx^2} - \frac{d \ln \rho}{dx} \frac{dX}{dx} - \frac{6}{x^2} X = 0, \tag{A22}$$

and

$$\frac{d^2 Y}{dx^2} - \frac{6}{x} \left(1 - \frac{\rho}{\bar{\rho}}\right) \frac{dY}{dx} - \frac{6}{x^2} \left(2\frac{\rho}{\bar{\rho}} - 1\right) Y = 0, \tag{A23}$$

in which $\bar{\rho} = 3m/(4\pi r^3)$ is the density of the material included inside radius r. The solutions of these equations are computed numerically

following the method presented in appendix B of Siess et al. (2013).

A2.3 Comparison with prescriptions in the literature

Within the MINT framework, we estimate each of the terms contributing to E_2 by evaluating the necessary structure quantities and integrals throughout grids of MESA models. We derive accurate E_2 for a wide range of masses, ages, and metallicities. These are shown in Fig. A8 for masses from 2 to $316 \, M_\odot$ at $Z = 0.02$. These models all feature a convective core surrounded by an extensive radiative zone in which low-frequency gravity waves dissipate energy. Points in the upper right corner of the plot show the age-independent BSE E_2 values (Hurley et al. 2002) for the same selection of masses. We note that the BSE prescription generally overestimates E_2. It roughly matches MINT at the ZAMS, but as evolution proceeds and the stellar convective core recedes, the MINT E_2 decreases by several orders of magnitude. The most massive stars see their structure change on the main sequence, starting with a convective core and a radiative surface, then developing a convective envelope as they inflate towards the end of the main sequence. This leads to a drop in E_2 in the late main-sequence matching the timing of the increase in E highlighted in Fig. A1. In those stars, the main tidal dissipation mechanism shifts from radiative to convective damping.

This is also an improvement on Siess et al. (2013), as their models yielded numerically noisy values and the corresponding prescription was expressed in the form of a set of fitting formulae of the mass and the metallicity.

Other prescriptions for E_2 found in the literature rely on the radius of the convective core, through scaling relations of the form

$$E_2 = 10^a \left(\frac{R_{\text{conv}}}{R}\right)^b, \tag{A24}$$

where Yoon et al. (2010) recommend $a = -1.37$, $b = 8$, while Qin et al. (2018) use $a = -0.42$, $b = 7.5$ for hydrogen-rich stars.

Fig. A9 presents a comparison between these prescriptions and our derivation for a $10 \, M_\odot$ star. While the prescription from Zahn (1989) matches our derivation of E_2 only at the ZAMS, other prescriptions all offer an agreement within one order of magnitude. Most notably, prescriptions relying on the convective core radius follow the same trend as our complete calculation and differ roughly by a multiplicative constant. Fig. A9 also shows two calculations relying on Siess et al. (2013): the dotted blue line relies on their fitting relation for the main-sequence lifetime (upon which E_2 strongly depends), while the solid blue line relies on the lifetimes obtained from our MESA runs. The difference in the lifetimes emerges from the use of two different mixing-length parameters in the models ($\alpha_{\text{MLT}} = 1.75$ in the models of Siess et al. 2013 and 2 in ours), along with updated equations of state and opacity tables in the MESA code on which our calculations rely.

APPENDIX B: POPULATION STUDIES FOR A RANGE OF OPEN CLUSTERS

In this appendix, we present the $e - \log_{10}(P/d)$ diagrams and statistics associated with the open clusters studied in Section 3.
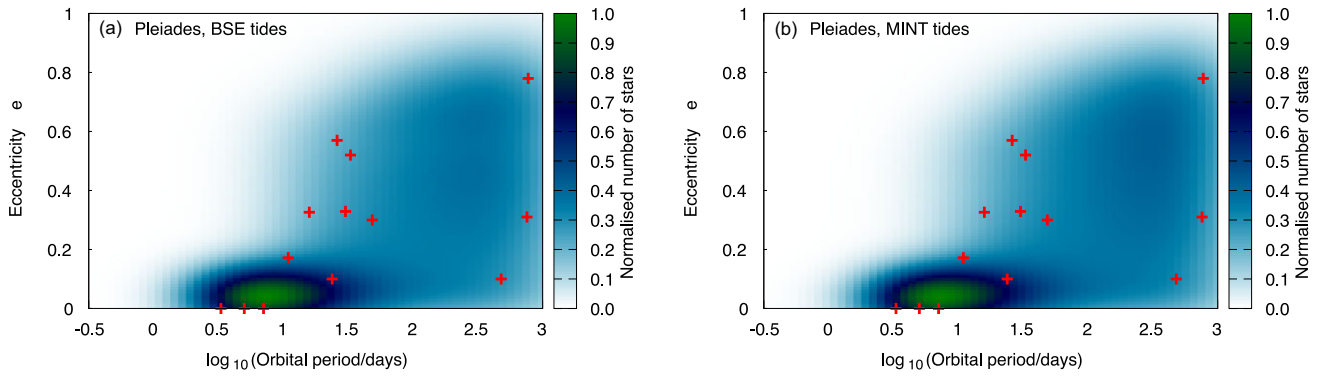
Figure B1. Comparison between Pleiades observations (red crosses) and the stellar counts calculated populations at the documented cluster age, normalized at the highest bin count (colour map). Starting from Moe & Di Stefano (2017) initial distributions, we test both BSE (a) and MINT (b) tidal prescriptions.
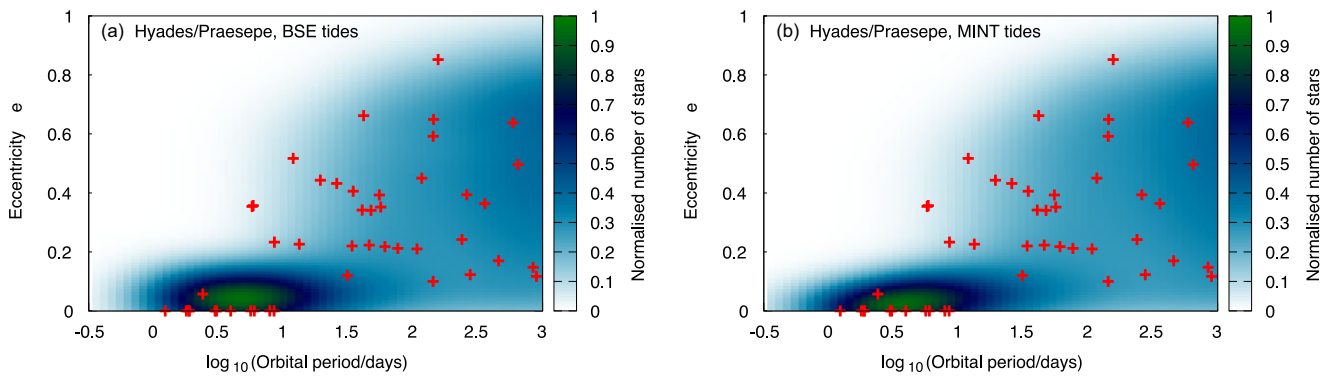
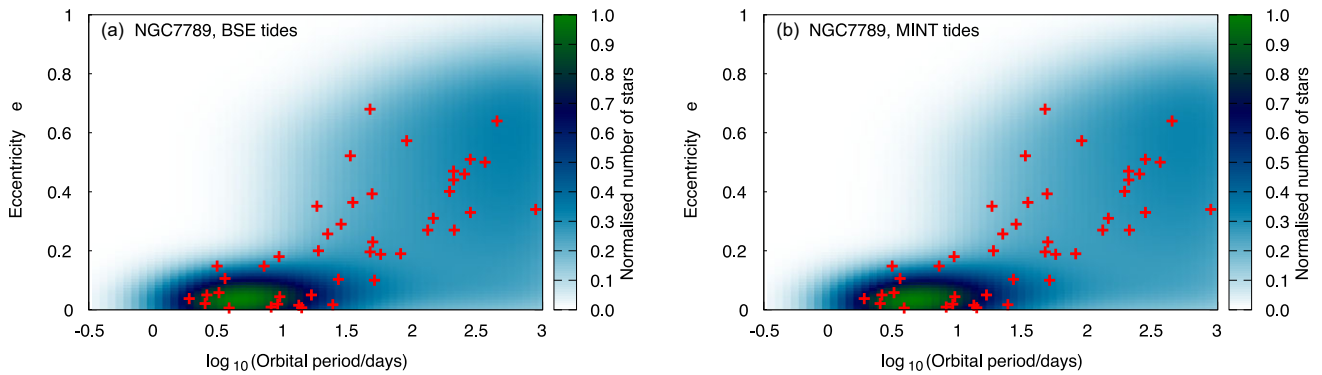**Figure B2.** As Fig. B1 for the Hyades and Praesepe twin clusters.

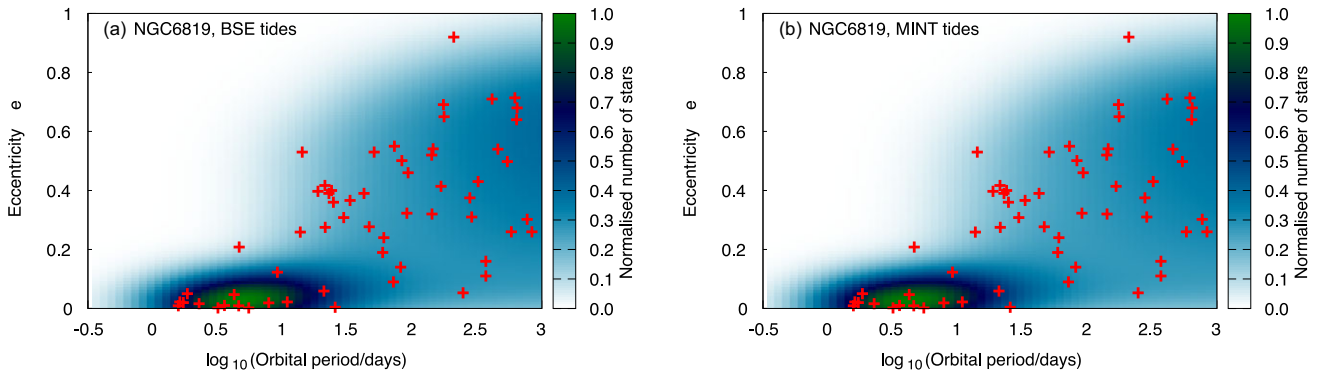**Figure B3.** As Fig. B1 for the NGC 7789 cluster.

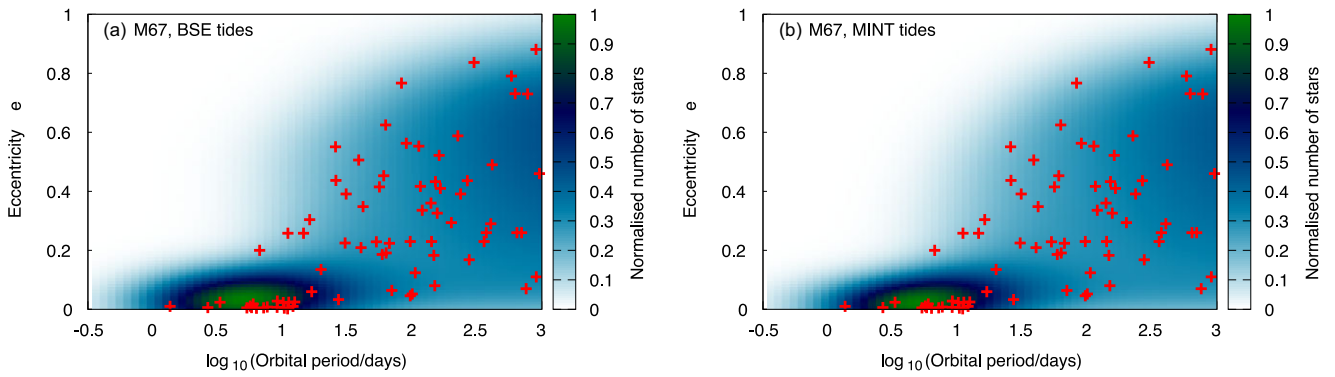**Figure B4.** As Fig. B1 for the NGC 6819 cluster.
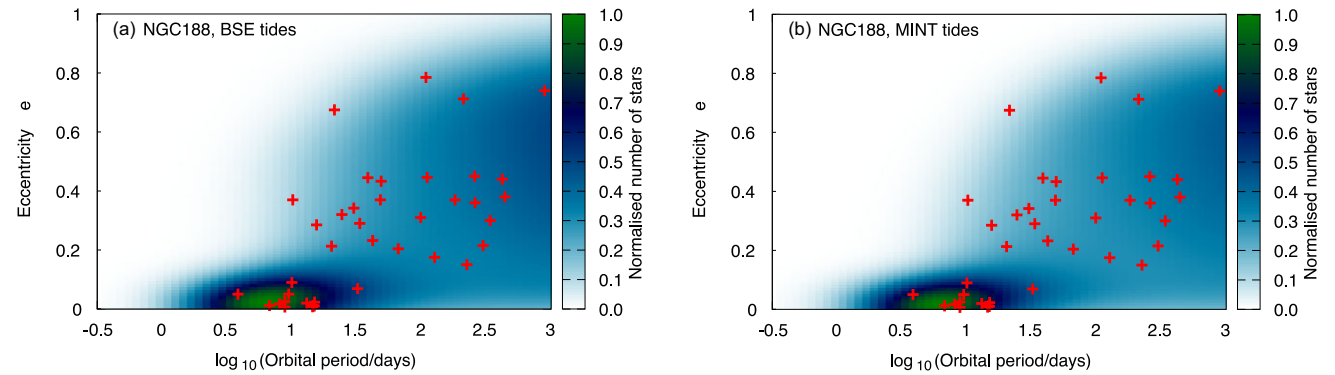

Figure B5. As Fig. B1 for the M67 cluster.

Figure B6. As Fig. B1 for the NGC 188 cluster.

This paper has been typeset from a TEX/LATEX file prepared by the author.